

Self-similar scaling and evolution in the galaxy cluster X-ray Luminosity-Temperature relation.

B. J. Maughan,^{1*} P. A. Giles,¹ S. W. Randall,² C. Jones,² and W. R. Forman²

¹*H. H. Wills Physics Laboratory, University of Bristol, Tyndall Ave, Bristol BS8 1TL, UK.*

²*Harvard-Smithsonian Center for Astrophysics, 60 Garden St, Cambridge, MA 02140, USA.*

25 February 2024

ABSTRACT

We investigate the form and evolution of the X-ray luminosity-temperature ($L_X - kT$) relation of a sample of 114 galaxy clusters observed with *Chandra* at $0.1 < z < 1.3$. The clusters were divided into subsamples based on their X-ray morphology or whether they host strong cool cores. We find that when the core regions are excluded, the most relaxed clusters (or those with the strongest cool cores) follow an $L_X - kT$ relation with a slope that agrees well with simple self-similar expectations. This is supported by an analysis of the gas density profiles of the systems, which shows self-similar behaviour of the gas profiles of the relaxed clusters outside the core regions. By comparing our data with clusters in the REXCESS sample, which extends to lower masses, we find evidence that the self-similar behaviour of even the most relaxed clusters breaks at around 3.5 keV. By contrast, the $L_X - kT$ slopes of the subsamples of unrelaxed systems (or those without strong cool cores) are significantly steeper than the self-similar model, with lower mass systems appearing less luminous and higher mass systems appearing more luminous than the self-similar relation. We argue that these results are consistent with a model of non-gravitational energy input in clusters that combines central heating with entropy enhancements from merger shocks. Such enhancements could extend the impact of central energy input to larger radii in unrelaxed clusters, as suggested by our data. We also examine the evolution of the $L_X - kT$ relation, and find that while the data appear inconsistent with simple self-similar evolution, the differences can be plausibly explained by selection bias, and thus we find no reason to rule out self-similar evolution. We show that the fraction of cool core clusters in our (non-representative) sample decreases at $z > 0.5$ and discuss the effect of this on measurements of the evolution in the $L_X - kT$ relation.

Key words: cosmology: observations – galaxies: clusters: general – galaxies: high-redshift – intergalactic medium – X-rays: galaxies

1 INTRODUCTION

The study of galaxy clusters is often motivated by one of two goals. First, clusters have been shown to be excellent cosmological probes, providing complementary and competitive constraints on cosmological parameters to those obtained using other techniques (e.g. Allen et al. 2008; Vikhlinin et al. 2009b). Second, galaxy clusters are unique laboratories in which to study extreme physical processes, such as cluster mergers or the interaction between relativistic jets from active galactic nuclei (AGN) and the X-ray emitting plasma of the intra-cluster medium (ICM). In fact these goals are not exclusive. Accurate cluster

mass measurements are required for cosmological studies, but these must be estimated from observable properties which can be strongly affected by the non-gravitational processes at play in clusters (Randall, Sarazin & Ricker 2002; Rowley, Thomas & Kay 2004; Kravtsov, Vikhlinin & Nagai 2006; Magliocchetti & Brüggen 2007; Hartley et al. 2008).

The scaling relations between different cluster observables and between those observables and cluster masses are a case in point. The relationships between readily observable cluster properties such as X-ray luminosity (L_X) or temperature (kT) and mass can often be approximated as simple power laws, and can be used to provide “cheap” mass estimates for large numbers of clusters out to high redshifts (Maughan 2007). Power law scaling relations are expected under simplified models in which clusters are self-similar ob-

* E-mail: ben.maughan@bristol.ac.uk

jects, having formed in single monolithic gravitational collapses and whose ICM is heated only by the shocks associated with the collapse (Kaiser 1986). In this self-similar model, galaxy clusters and groups of all masses are identical objects when scaled by their mass. This is referred to as *strong* self-similarity (Bower 1997), and sets the power law slopes of the scaling relations which are not predicted to evolve with redshift. Evolution is expected, however, in the normalisation of the scaling relations, and is due (in the self-similar model) solely to the changing density of the Universe with redshift (Bryan & Norman 1998). This redshift-dependent evolution in the normalisation of the scaling relations is referred to as *weak* self-similarity.

The $L_X - kT$ relation is the most well studied of these scaling relations (e.g. Mitchell et al. 1979; Mushotzky 1984; Edge & Stewart 1991; Markevitch 1998; Ettori et al. 2004; Pratt et al. 2009; Mittal et al. 2011), as these two properties can easily be measured directly and essentially independently from X-ray data. Indeed, the observational consensus is that the slope of the $L_X - kT$ relation is ~ 3 , significantly steeper than the self-similar prediction of 2, and appears to steepen further at galaxy group scales (e.g. Helsdon & Ponman 2000; Osmond & Ponman 2004). The slope of the $L_X - kT$ relation is the archetypal example of the departure of clusters from the self-similar predictions. Other evidence for similarity breaking is seen in the radial distribution of the ICM. Using simple models, Neumann & Arnaud (1999) found evidence for self-similarity of cluster surface brightness profiles outside the core regions, and Arnaud, Aghanim & Neumann (2002) extended this result to higher redshift clusters. Ponman, Cannon & Navarro (1999) showed that surface brightness profiles of the hotter (> 4 keV) clusters in their sample of relaxed systems were self similar outside of the core regions. Recently, with higher-quality data and more sophisticated modelling, the picture has become more detailed; Croston et al. (2008) used *XMM-Newton* observations to examine the gas density profiles of a representative sample of 31 local clusters and found that outside the core regions there is a temperature dependence of the gas density profiles, but at larger radii, the profiles become self-similar for the most massive clusters. Using the same sample of clusters, (Arnaud et al. 2010) also showed that the pressure profiles of the ICM have a universal, self-similar form, with low dispersion outside the core regions.

Perhaps the most detailed information on the processes responsible for similarity breaking has come from observations of the entropy distribution of the ICM. Entropy is useful in this regard because it is conserved in adiabatic processes, and so provides a good indicator of the thermal history of the gas. A key observation has been that the entropy profiles of galaxy groups and clusters show departures from a self-similar power law, with profiles flattening in the core regions, indicating an absence of the expected low-entropy gas in cluster cores (e.g. Ponman, Cannon & Navarro 1999; Voit, Kay & Bryan 2005; Pratt et al. 2010). As this low-entropy gas is also the most luminous part of the ICM, a mechanism that removed or raised the entropy of this gas, and that had a proportionately larger effect in low mass systems, would also in principal explain the steeper than self-similar slope of the $L_X - kT$ relation, and the similarity breaking in ICM density profiles.

A great deal of work has been performed in investigating the different processes that could be responsible for this similarity breaking, with cooling out of the low entropy gas (e.g. Bryan 2000), preheating (energy input at early times in the formation of clusters; e.g. Borgani et al. 2002), and energy input from supernovae-driven galactic outflows all considered. A consensus is now emerging that energy input from AGN at high redshift, when they are in quasar-mode with high accretion rates, are responsible for providing a roughly constant (with halo mass) level of entropy injection to the ICM, leading to the observed ICM structure and scaling relations (e.g. Bower, McCarthy & Benson 2008; Short & Thomas 2009; McCarthy et al. 2011).

Any study of the $L_X - kT$ relation must include a consideration of the phenomenon of cool cores in clusters. These dense, cool regions in the centres of many clusters radiate efficiently in X-rays, and were long thought to be the sites of deposition of large quantities (hundreds of solar masses per year) of condensed ICM (see Fabian 1994, for a review). High resolution X-ray spectroscopy subsequently revealed that gas was not cooling out of the X-ray emitting phase in the large quantities predicted, with the bulk of it instead stabilising at around $1/3$ of the global temperature (Peterson et al. 2001; Kaastra et al. 2001; David et al. 2001). This effectively substituted the problem of explaining the fate of the cooling gas with the need for a mechanism to balance the cooling process to give the observed, lower cooling rates. This problem has been vigorously investigated over the past decade, with energy input from AGN emerging as the most likely candidate (e.g. McNamara & Nulsen 2007). This is a milder form of AGN input than the quasar-mode heating that drives similarity breaking. Here the energy is thought to be input to the ICM via the bubbles inflated by the AGN jets and associated weak shocks, with the energy input coupled to the cooling rate by some feedback mechanism to maintain a rough balance between heating and cooling. Cool cores also have an important observational effect in that they significantly increase (decrease) the measured global L_X (kT) compared to clusters without cool cores. The presence and strength of cool cores can thus influence the detectability of clusters in X-ray surveys, and complicate measurements of the form and evolution of the $L_X - kT$ relation (and are a dominant source of scatter in luminosity scaling relations).

Knowledge of the evolution of the $L_X - kT$ relation is important as a step in the process of providing mass estimates for high- z clusters, understanding the selection functions of X-ray cluster surveys, and also for probing the history of the heating mechanisms in clusters. For example, simulations have shown that AGN heating and preheating models give divergent predictions for the evolution of the $L_X - kT$ relation, allowing the models to be distinguished observationally (Short et al. 2010). Observational results are somewhat mixed, with some studies finding that evolution to $z \sim 1$ is consistent with self-similar predictions in which the evolution is driven by the increasing density of the Universe with redshift, leading to denser collapsed objects (e.g. Vikhlinin et al. 2002; Lumb et al. 2004; Maughan et al. 2006), while other studies have found evidence for departures from self-similar evolution (e.g. Ettori et al. 2004; Branchesi et al. 2007). Recent work, however, has demonstrated the importance of considering selection bias in stud-

ies of the evolution of L_X scaling relations, showing that such biases can mimic or reduce sensitivity to departures from self-similar evolution (Stanek et al. 2006; Pacaud et al. 2007; Nord et al. 2008; Mantz et al. 2010a).

In this paper we investigate the $L_X - kT$ relation of a sample of 114 clusters covering wide temperature ($2 < kT < 16$ keV) and redshift ($0.1 < z < 1.3$) baselines to examine the strong and weak self-similarity of the cluster population. The sample was first presented in Maughan et al. (2008, hereafter M08), wherein the analysis methods were described, and the evolution of the structural properties and metal abundance were investigated. Subsequently the sample was used to show that L_X is a more precise mass estimator than had previously been thought (Maughan 2007). The current paper is organised as follows: in §2 we review the sample and describe updates to the analysis and calibration of the data since Maughan et al. (2008); in §3 we discuss the classification of clusters based on dynamical and cool core state; in §4 and §5 respectively, strong and weak self-similarity are investigated, and in §6 and §7 the results are discussed and our conclusions are summarised. A Λ CDM cosmology of $H_0 = 70 \text{ km s}^{-1} \text{ Mpc}^{-1}$ ($\equiv 100h \text{ km s}^{-1} \text{ Mpc}^{-1}$, and $\Omega_M = 0.3$ ($\Omega_\Lambda = 0.7$) is adopted throughout and all errors are quoted at the 68% confidence level.

2 SAMPLE AND DATA REDUCTION

The sample used for this study is a set of 114 galaxy clusters covering the redshift range $0.1 < z < 1.3$ observed with *Chandra* ACIS-I, and originally presented in M08. In this work, the data have been reanalysed using updated versions of the *CIAO* software package (version 4.2), and the *Chandra* Calibration Database (version 4.3.0). The full analysis procedure is as described in M08, but the key steps are summarised in the following, along with any differences in procedure from that work.

The data were reprocessed from the level 1 events and cleaned and filtered. Blank-sky background files appropriate for each observation were also prepared and normalised to match the 9.5 – 12 keV count rate in the cluster data. Point sources were detected and excluded from all further analysis. The X-ray centroid of the cluster was determined, and radial profiles of the cluster and background data were used to determine the extent of the cluster emission, and to define local background regions free from cluster emission. Spectra were extracted from the cluster and blank-sky files in these local background regions and used to measure the difference in soft Galactic emission between the cluster and blank-sky data. This difference spectrum was fit with a soft APEC (Smith et al. 2001) plasma model and included as a fixed component in the spectral fits to the cluster spectra, with the normalisation scaled by extraction area (see Vikhlinin et al. 2005, for details). Fits to the cluster spectra were performed in the 0.6 – 9 keV band with an absorbed APEC model, with the absorbing column fixed at the Galactic value (Dickey & Lockman 1990).

The gas density profile of each cluster was determined by converting the observed surface brightness profile (measured in the 0.7 – 2 keV band) into a projected emissivity profile, which was then modelled by projecting a density

model along the line of sight (see M08 for details). The model used was that of Vikhlinin et al. (2006b, see that work for definitions of the parameters);

$$n_p n_e = \frac{n_0^2 (r/r_c)^{-\alpha}}{(1 + r^2/r_c^2)^{3\beta-\alpha/2}} \times (1 + r^\gamma/r_s^\gamma)^{-\epsilon/\gamma}, \quad (1)$$

a modification of the widely used β -model, with added flexibility to fit a power law cusp in the core and a change in slope at large radii. Gas masses were then determined from Monte Carlo realisations of the projected emissivity profile based on the best fitting projected model to the original data. At each data point, a new randomised point was drawn from a Gaussian distribution centered on the model value at that point, with a standard deviation equal to the fractional measurement error on the original data point, multiplied by the model value. Note that this represents a minor change from M08 in which we randomised the original *data* to derive the uncertainties on the model parameters. The new approach is considered superior as we avoid adding noise to an already noisy observed profile.

The cluster temperature, gas mass and R_{500} (the radius enclosing a mean density of 500 times the critical density at the cluster’s redshift) were then determined iteratively. The procedure followed was to extract a spectrum from within an estimated R_{500} (with the central 15% of that radius excluded), integrate the gas density profile to determine the gas mass within the estimated R_{500} , and thus calculate Y_X (the product of kT and the gas mass, and a low scatter proxy for total mass Kravtsov, Vikhlinin & Nagai 2006). A new value of R_{500} was then estimated from the Y_X -M scaling relation of Vikhlinin et al. (2009a),

$$M_{500} = E^{-2/5}(z) A_{YM} \frac{Y_X^{B_{YM}}}{3 \times 10^{14} M_\odot \text{ keV}}, \quad (2)$$

with $A_{YM} = 5.77 \times 10^{14} h^{1/2} M_\odot$ and $B_{YM} = 0.57$. Here, M_{500} is the mass within R_{500} (allowing R_{500} to be trivially computed), and $E(z) = \sqrt{\Omega_M(1+z)^3 + (1 - \Omega_M - \Omega_\Lambda)(1+z)^2 + \Omega_\Lambda}$, describing the redshift evolution of the Hubble parameter. This $Y_X - M_{500}$ relation assumes self-similar evolution (as $E^{-2/5}$), which has been shown to be a good description of observed clusters to $z \approx 0.6$ (Maughan 2007). Equation (2) is an updated version of the Y_X -M relation used in M08, but the change is negligible here, leading to a $\lesssim 2\%$ increase in R_{500} for the range of masses considered here. The process was repeated until R_{500} converged. The temperature and luminosity were then measured from spectra extracted within R_{500} both with and without the central 15% of that radius excluded. We use the notation $L_{X,\text{tot}}$ and kT_{tot} to indicate properties measured in the $(0 - 1)R_{500}$ aperture and $L_{X,c}$ and kT_c for those in the core-excised $(0.15 - 1)R_{500}$ aperture.

The measured properties of the clusters are given in Table 1. All luminosities are bolometric.

2.1 Comparison with M08

In addition to the general methodological differences between M08 and the current work that are described above, some improvements were made to the analyses of specific clusters. Specifically, for several clusters additional light-

Table 1: Summary of cluster properties. $L_{X,\text{tot}}$ and kT_{tot} were measured in the $(0 - 1)R_{500}$ aperture and $L_{X,c}$ and kT_c were measured in the $(0.15 - 1)R_{500}$ aperture. Clusters are in order of right ascension, and luminosities are bolometric.

Cluster	z	R_{500} (Mpc)	kT_{tot} (keV)	$L_{X,\text{tot}}$ (10^{44} erg s $^{-1}$)	kT_c (keV)	$L_{X,c}$ (10^{44} erg s $^{-1}$)
MS0015.9+1609	0.541	1.26	$8.3^{+0.4}_{-0.3}$	50.6 ± 0.6	$8.3^{+0.5}_{-0.4}$	35.5 ± 0.5
RXJ0027.6+2616	0.367	0.99	$5.2^{+1.3}_{-0.7}$	7.4 ± 0.5	$4.8^{+1.0}_{-0.8}$	5.6 ± 0.5
CLJ0030+2618	0.500	0.84	$4.1^{+0.6}_{-0.8}$	4.9 ± 0.9	$4.1^{+1.7}_{-1.0}$	3.6 ± 0.8
A68	0.255	1.25	$8.6^{+1.0}_{-0.5}$	17.7 ± 0.5	$7.8^{+1.0}_{-1.0}$	10.4 ± 0.4
A115	0.197	1.28	$5.3^{+0.1}_{-0.1}$	13.7 ± 0.1	$6.7^{+0.3}_{-0.3}$	9.7 ± 0.1
A209	0.206	1.34	$7.2^{+0.4}_{-0.4}$	19.2 ± 0.3	$7.4^{+0.5}_{-0.5}$	13.1 ± 0.2
CLJ0152.7-1357S	0.831	0.76	$4.6^{+0.8}_{-0.7}$	9.1 ± 0.6	$4.9^{+1.1}_{-0.9}$	7.1 ± 0.6
A267	0.230	1.07	$4.9^{+0.3}_{-0.3}$	12.4 ± 0.6	$4.4^{+0.5}_{-0.4}$	7.3 ± 0.5
CLJ0152.7-1357N	0.831	0.78	$5.1^{+0.7}_{-0.7}$	11.8 ± 0.6	$4.9^{+0.9}_{-0.8}$	9.6 ± 0.8
MACSJ0159.8-0849	0.405	1.32	$7.9^{+0.3}_{-0.3}$	42.0 ± 0.5	$10.2^{+0.9}_{-0.9}$	19.0 ± 0.4
CLJ0216-1747	0.578	0.78	$5.9^{+2.9}_{-1.7}$	2.8 ± 0.3	$5.6^{+3.8}_{-1.8}$	2.1 ± 0.2
RXJ0232.2-4420	0.284	1.33	$6.5^{+0.5}_{-0.4}$	30.7 ± 0.9	$8.0^{+1.4}_{-1.1}$	16.7 ± 0.7
MACSJ0242.5-2132	0.314	1.08	$4.6^{+0.2}_{-0.2}$	28.4 ± 0.7	$5.5^{+0.7}_{-0.6}$	7.8 ± 0.3
A383	0.187	1.03	$3.9^{+0.1}_{-0.1}$	9.9 ± 0.2	$4.5^{+0.3}_{-0.3}$	3.8 ± 0.1
MACSJ0257.6-2209	0.322	1.17	$7.2^{+0.6}_{-0.5}$	17.3 ± 0.4	$6.7^{+0.9}_{-0.6}$	8.7 ± 0.3
MS0302.7+1658	0.424	0.81	$3.4^{+0.5}_{-0.4}$	6.3 ± 0.7	$3.3^{+0.8}_{-0.6}$	3.2 ± 0.7
CLJ0318-0302	0.370	0.94	$5.4^{+1.2}_{-0.9}$	6.0 ± 0.4	$5.4^{+1.7}_{-1.2}$	3.9 ± 0.3
MACSJ0329.6-0211	0.450	1.01	$4.5^{+0.2}_{-0.3}$	28.6 ± 0.8	$4.5^{+0.5}_{-0.4}$	11.6 ± 0.5
MACSJ0404.6+1109	0.355	1.09	$5.8^{+0.6}_{-0.5}$	10.8 ± 0.4	$5.5^{+0.7}_{-0.5}$	8.7 ± 0.4
MACSJ0429.6-0253	0.399	1.08	$5.2^{+0.2}_{-0.2}$	24.5 ± 0.6	$6.5^{+0.9}_{-0.7}$	9.3 ± 0.4
RXJ0439.0+0715	0.230	1.14	$5.4^{+0.3}_{-0.2}$	16.1 ± 0.3	$5.3^{+0.4}_{-0.3}$	8.7 ± 0.3
RXJ0439+0520	0.208	0.97	$3.7^{+0.2}_{-0.2}$	9.3 ± 0.4	$3.9^{+0.4}_{-0.4}$	3.3 ± 0.3
MACSJ0451.9+0006	0.430	1.02	$5.8^{+0.7}_{-0.9}$	16.9 ± 0.8	$5.0^{+1.1}_{-0.6}$	11.1 ± 0.7
A521	0.253	1.20	$4.9^{+0.2}_{-0.2}$	16.4 ± 0.3	$4.8^{+0.2}_{-0.2}$	13.8 ± 0.3
A520	0.199	1.31	$6.6^{+0.2}_{-0.2}$	18.4 ± 0.2	$6.5^{+0.3}_{-0.3}$	14.5 ± 0.2
MS0451.6-0305	0.550	1.19	$6.8^{+0.8}_{-0.6}$	46.8 ± 1.9	$7.6^{+1.2}_{-1.0}$	31.3 ± 1.6
CLJ0522-3625	0.472	0.82	$4.3^{+1.0}_{-0.9}$	3.3 ± 0.3	$4.3^{+1.4}_{-1.0}$	2.5 ± 0.2
CLJ0542.8-4100	0.642	0.91	$6.4^{+0.8}_{-0.7}$	11.3 ± 0.5	$6.2^{+1.0}_{-0.8}$	8.6 ± 0.4
MACSJ0647.7+7015	0.584	1.26	$10.9^{+1.4}_{-0.9}$	43.8 ± 1.1	$11.3^{+2.1}_{-1.6}$	24.7 ± 0.8
1E0657-56	0.296	1.64	$11.5^{+0.4}_{-0.4}$	79.3 ± 0.6	$11.7^{+0.5}_{-0.5}$	55.4 ± 0.5
MACSJ0717.5+3745	0.546	1.40	$11.2^{+0.7}_{-0.7}$	79.3 ± 1.2	$10.6^{+1.0}_{-0.6}$	59.0 ± 0.9
A586	0.171	1.23	$7.2^{+0.5}_{-0.5}$	15.2 ± 0.4	$7.6^{+0.8}_{-0.8}$	7.6 ± 0.4
MACSJ0744.9+3927	0.697	1.08	$7.7^{+0.4}_{-0.4}$	48.9 ± 0.9	$8.1^{+0.7}_{-0.6}$	25.1 ± 0.7
A665	0.182	1.42	$7.5^{+0.3}_{-0.3}$	23.4 ± 0.3	$7.8^{+0.4}_{-0.4}$	16.6 ± 0.2
A697	0.282	1.49	$9.8^{+0.5}_{-0.5}$	40.4 ± 0.6	$10.2^{+0.8}_{-0.7}$	26.4 ± 0.5
CLJ0848.7+4456	0.574	0.57	$2.4^{+0.4}_{-0.3}$	1.1 ± 0.2	$2.0^{+0.2}_{-0.3}$	0.9 ± 0.2
ZWCLJ1953	0.320	1.14	$7.0^{+0.6}_{-0.6}$	16.4 ± 0.4	$6.1^{+0.6}_{-0.6}$	9.3 ± 0.3
CLJ0853+5759	0.475	0.83	$5.0^{+1.3}_{-0.9}$	3.0 ± 0.4	$5.1^{+1.5}_{-0.9}$	2.6 ± 0.4
MS0906.5+1110	0.180	1.10	$5.2^{+0.2}_{-0.2}$	9.0 ± 0.2	$4.7^{+0.3}_{-0.3}$	5.0 ± 0.1
RXJ0910+5422	1.110	0.48	$4.6^{+1.4}_{-1.1}$	2.8 ± 0.3	$2.7^{+1.9}_{-0.8}$	2.2 ± 0.4
A773	0.217	1.30	$7.5^{+0.3}_{-0.3}$	18.3 ± 0.3	$7.4^{+0.4}_{-0.4}$	11.4 ± 0.2
A781	0.298	1.14	$5.5^{+0.6}_{-0.6}$	11.8 ± 0.5	$5.5^{+0.7}_{-0.5}$	9.9 ± 0.5
CLJ0926+1242	0.489	0.84	$4.0^{+0.5}_{-0.4}$	4.6 ± 0.3	$4.5^{+1.0}_{-0.9}$	3.2 ± 0.3
RBS797	0.354	1.19	$6.2^{+0.3}_{-0.3}$	50.3 ± 0.9	$7.3^{+1.0}_{-0.9}$	13.0 ± 0.6
MACSJ0949.8+1708	0.384	1.24	$7.5^{+0.6}_{-0.6}$	28.6 ± 0.7	$7.3^{+0.9}_{-0.8}$	17.4 ± 0.6
CLJ0956+4107	0.587	0.81	$4.8^{+0.8}_{-0.7}$	5.8 ± 0.3	$4.0^{+0.7}_{-0.5}$	4.5 ± 0.4
A907	0.153	1.14	$5.2^{+0.1}_{-0.4}$	11.5 ± 0.1	$5.4^{+0.2}_{-0.2}$	5.1 ± 0.1
MS1006.0+1202	0.221	1.12	$5.6^{+0.5}_{-0.5}$	7.7 ± 0.2	$6.0^{+0.5}_{-0.5}$	5.1 ± 0.2
MS1008.1-1224	0.301	1.04	$5.0^{+0.3}_{-0.3}$	10.4 ± 0.3	$4.6^{+0.4}_{-0.4}$	6.7 ± 0.3
ZW3146	0.291	1.28	$6.2^{+0.1}_{-0.1}$	47.0 ± 0.4	$7.8^{+0.4}_{-0.4}$	16.3 ± 0.3
CLJ1113.1-2615	0.725	0.65	$3.8^{+0.8}_{-0.6}$	3.8 ± 0.4	$3.6^{+1.3}_{-0.8}$	2.4 ± 0.5
A1204	0.171	0.96	$3.4^{+0.1}_{-0.1}$	9.9 ± 0.2	$3.7^{+0.3}_{-0.3}$	2.7 ± 0.1
CLJ1117+1745	0.548	0.71	$3.1^{+0.6}_{-0.5}$	2.1 ± 0.3	$3.3^{+0.9}_{-0.6}$	1.8 ± 0.2
CLJ1120+4318	0.600	0.93	$5.8^{+0.9}_{-0.7}$	13.4 ± 0.8	$5.2^{+1.3}_{-0.8}$	8.7 ± 0.7
RXJ1121+2327	0.562	0.78	$3.5^{+0.3}_{-0.3}$	5.0 ± 0.3	$3.2^{+0.3}_{-0.3}$	4.3 ± 0.3

continued on next page

Table 1: *continued*

Cluster	z	R_{500} (Mpc)	kT_{tot} (keV)	$L_{X,\text{tot}}$ ($10^{44} \text{ erg s}^{-1}$)	kT_c (keV)	$L_{X,c}$ ($10^{44} \text{ erg s}^{-1}$)
A1240	0.159	0.92	$3.8^{+0.3}_{-0.3}$	1.8 ± 0.1	$3.8^{+0.3}_{-0.3}$	1.6 ± 0.1
MACSJ1131.8-1955	0.307	1.43	$8.1^{+0.9}_{-0.7}$	31.5 ± 1.0	$9.5^{+1.8}_{-1.4}$	21.9 ± 0.9
MS1137.5+6625	0.782	0.83	$6.6^{+0.8}_{-0.7}$	14.0 ± 0.5	$6.5^{+1.2}_{-1.0}$	7.9 ± 0.4
MACSJ1149.5+2223	0.545	1.28	$9.3^{+0.9}_{-0.8}$	47.2 ± 1.2	$8.5^{+1.1}_{-0.7}$	35.3 ± 1.1
A1413	0.143	1.30	$7.2^{+0.2}_{-0.2}$	17.1 ± 0.1	$7.1^{+0.3}_{-0.3}$	8.6 ± 0.1
CLJ1213+0253	0.409	0.79	$3.5^{+0.7}_{-0.6}$	2.1 ± 0.6	$3.9^{+0.9}_{-0.8}$	1.6 ± 0.5
RXJ1221+4918	0.700	0.90	$6.2^{+0.6}_{-0.6}$	12.6 ± 0.4	$5.9^{+0.7}_{-0.7}$	10.1 ± 0.4
CLJ1226.9+3332	0.890	0.97	$10.3^{+1.3}_{-0.9}$	45.3 ± 1.3	$10.0^{+1.9}_{-1.4}$	24.5 ± 1.1
RXJ1234.2+0947	0.229	1.15	$6.6^{+2.3}_{-1.2}$	6.2 ± 0.4	$7.6^{+2.4}_{-2.0}$	5.5 ± 0.3
RDCS1252-29	1.237	0.55	$4.7^{+0.9}_{-0.7}$	6.5 ± 0.7	$4.6^{+0.9}_{-0.7}$	5.4 ± 0.7
A1682	0.234	1.20	$6.1^{+1.3}_{-1.0}$	12.4 ± 1.4	$5.8^{+2.0}_{-1.2}$	9.7 ± 1.2
MACSJ1311.0-0310	0.494	0.97	$5.5^{+0.3}_{-0.2}$	17.7 ± 0.3	$6.5^{+0.8}_{-0.6}$	7.2 ± 0.2
A1689	0.183	1.40	$9.0^{+0.3}_{-0.3}$	39.4 ± 0.3	$8.4^{+0.4}_{-0.3}$	15.7 ± 0.2
RXJ1317.4+2911	0.805	0.51	$2.4^{+0.7}_{-0.6}$	1.1 ± 0.3	$2.2^{+0.8}_{-0.4}$	0.9 ± 0.7
CLJ1334+5031	0.620	0.88	$4.6^{+1.3}_{-1.2}$	7.6 ± 0.9	$5.2^{+2.1}_{-1.5}$	5.8 ± 0.7
A1763	0.223	1.38	$8.1^{+0.4}_{-0.4}$	21.3 ± 0.3	$8.1^{+0.5}_{-0.5}$	14.5 ± 0.3
RXJ1347.5-1145	0.451	1.51	$12.6^{+0.4}_{-0.4}$	155.6 ± 1.4	$14.2^{+1.4}_{-1.4}$	44.1 ± 0.8
RXJ1350.0+6007	0.804	0.72	$4.2^{+0.9}_{-0.7}$	5.5 ± 0.5	$4.5^{+1.0}_{-0.8}$	4.6 ± 0.5
CLJ1354-0221	0.546	0.74	$3.8^{+0.7}_{-0.6}$	3.6 ± 0.3	$3.1^{+0.9}_{-0.5}$	3.0 ± 0.3
CLJ1415.1+3612	1.030	0.65	$5.3^{+0.7}_{-0.6}$	11.9 ± 0.7	$4.3^{+0.6}_{-0.6}$	7.5 ± 0.6
RXJ1416+4446	0.400	0.87	$3.5^{+0.3}_{-0.2}$	5.9 ± 0.5	$3.9^{+0.5}_{-0.4}$	3.6 ± 0.4
MACSJ1423.8+2404	0.543	1.01	$6.2^{+0.5}_{-0.4}$	31.6 ± 1.0	$6.0^{+1.0}_{-0.8}$	12.0 ± 0.7
A1914	0.171	1.40	$9.6^{+0.3}_{-0.3}$	34.3 ± 0.3	$8.5^{+0.4}_{-0.4}$	14.0 ± 0.2
A1942	0.224	0.97	$4.6^{+0.3}_{-0.3}$	4.0 ± 0.1	$4.2^{+0.3}_{-0.3}$	3.0 ± 0.1
MS1455.0+2232	0.258	1.07	$4.5^{+0.1}_{-0.1}$	21.9 ± 0.2	$4.7^{+0.2}_{-0.2}$	6.4 ± 0.1
RXJ1504-0248	0.215	1.40	$7.1^{+0.2}_{-0.2}$	66.6 ± 0.7	$9.4^{+1.1}_{-1.0}$	15.1 ± 0.5
A2034	0.113	1.23	$6.6^{+0.1}_{-0.2}$	9.4 ± 0.1	$6.3^{+0.2}_{-0.2}$	6.6 ± 0.1
A2069	0.116	1.21	$6.0^{+0.2}_{-0.2}$	6.4 ± 0.1	$5.9^{+0.3}_{-0.3}$	5.5 ± 0.1
RXJ1525+0958	0.516	0.84	$3.7^{+0.3}_{-0.3}$	6.7 ± 0.4	$3.5^{+0.3}_{-0.4}$	5.7 ± 0.4
RXJ1532.9+3021	0.345	1.14	$5.1^{+0.2}_{-0.2}$	38.0 ± 0.9	$6.3^{+1.0}_{-0.8}$	11.7 ± 0.5
A2111	0.229	1.23	$6.4^{+0.6}_{-0.5}$	11.4 ± 0.3	$6.4^{+0.7}_{-0.6}$	8.3 ± 0.3
A2125	0.246	0.79	$2.5^{+0.1}_{-0.1}$	2.0 ± 0.1	$2.4^{+0.2}_{-0.2}$	1.7 ± 0.1
A2163	0.203	1.91	$14.7^{+0.8}_{-0.9}$	93.9 ± 1.3	$15.2^{+1.2}_{-1.2}$	58.6 ± 1.2
MACSJ1621.3+3810	0.463	1.03	$6.1^{+0.3}_{-0.3}$	19.8 ± 0.6	$6.2^{+0.5}_{-0.5}$	9.2 ± 0.5
MS1621.5+2640	0.426	1.04	$6.1^{+0.6}_{-0.6}$	11.2 ± 0.4	$5.8^{+0.7}_{-0.6}$	8.7 ± 0.4
A2204	0.152	1.44	$7.1^{+0.2}_{-0.2}$	41.1 ± 0.4	$8.4^{+0.8}_{-0.6}$	13.1 ± 0.3
A2218	0.176	1.21	$6.4^{+0.2}_{-0.2}$	13.3 ± 0.1	$6.0^{+0.3}_{-0.3}$	8.3 ± 0.1
CLJ1641+4001	0.464	0.77	$3.5^{+0.4}_{-0.4}$	2.7 ± 0.3	$3.5^{+0.6}_{-0.5}$	2.0 ± 0.3
RXJ1701+6414	0.453	0.88	$3.8^{+0.3}_{-0.3}$	6.8 ± 0.6	$4.1^{+0.5}_{-0.4}$	4.5 ± 0.6
RXJ1716.9+6708	0.813	0.81	$6.3^{+1.0}_{-0.8}$	13.5 ± 0.7	$5.7^{+1.1}_{-0.9}$	9.0 ± 0.7
A2259	0.164	1.11	$5.2^{+0.3}_{-0.3}$	8.8 ± 0.2	$5.2^{+0.4}_{-0.4}$	5.3 ± 0.2
RXJ1720.1+2638	0.164	1.27	$5.9^{+0.1}_{-0.1}$	22.3 ± 0.2	$6.8^{+0.5}_{-0.3}$	8.4 ± 0.2
MACSJ1720.2+3536	0.387	1.15	$6.2^{+0.4}_{-0.3}$	25.6 ± 0.6	$7.2^{+0.9}_{-0.8}$	11.5 ± 0.4
A2261	0.224	1.34	$7.3^{+0.2}_{-0.2}$	29.1 ± 0.3	$7.3^{+0.4}_{-0.4}$	14.3 ± 0.2
A2294	0.178	1.35	$8.9^{+0.8}_{-0.7}$	15.4 ± 0.4	$8.4^{+1.1}_{-0.8}$	9.4 ± 0.3
MACSJ1824.3+4309	0.487	0.90	$4.1^{+0.9}_{-0.6}$	5.7 ± 0.7	$4.8^{+1.4}_{-0.9}$	4.5 ± 0.5
MACSJ1931.8-2634	0.352	1.22	$5.9^{+0.3}_{-0.3}$	46.8 ± 0.9	$6.7^{+1.1}_{-0.7}$	14.7 ± 0.5
RXJ2011.3-5725	0.279	0.89	$4.0^{+0.2}_{-0.2}$	6.9 ± 0.3	$3.6^{+0.4}_{-0.4}$	3.0 ± 0.2
MS2053.7-0449	0.583	0.76	$4.0^{+0.4}_{-0.4}$	4.9 ± 0.3	$3.9^{+0.6}_{-0.5}$	3.1 ± 0.3
MACSJ2129.4-0741	0.594	1.12	$8.9^{+1.1}_{-0.7}$	37.2 ± 1.2	$8.3^{+1.1}_{-1.1}$	22.3 ± 1.0
RXJ2129.6+0005	0.235	1.22	$5.2^{+0.2}_{-0.2}$	21.4 ± 0.5	$6.2^{+0.6}_{-0.6}$	9.8 ± 0.4
A2409	0.148	1.18	$5.5^{+0.3}_{-0.2}$	11.5 ± 0.2	$5.7^{+0.4}_{-0.4}$	6.7 ± 0.2
MACSJ2228.5+2036	0.412	1.29	$8.2^{+0.7}_{-0.6}$	33.4 ± 0.8	$8.6^{+1.4}_{-0.8}$	22.2 ± 0.7
MACSJ2229.7-2755	0.324	1.03	$4.1^{+0.2}_{-0.2}$	20.5 ± 0.8	$5.0^{+0.9}_{-0.7}$	6.4 ± 0.4
MACSJ2245.0+2637	0.301	1.05	$5.2^{+0.3}_{-0.3}$	17.1 ± 0.5	$4.9^{+0.5}_{-0.5}$	6.8 ± 0.4
RXJ2247+0337	0.200	0.67	$2.7^{+0.7}_{-0.5}$	0.4 ± 0.1	$2.9^{+0.9}_{-0.6}$	0.3 ± 0.1
AS1063	0.348	1.56	$11.5^{+0.6}_{-0.6}$	93.6 ± 1.1	$11.2^{+1.1}_{-0.9}$	42.1 ± 0.9
CLJ2302.8+0844	0.722	0.76	$5.4^{+1.5}_{-1.0}$	5.2 ± 0.4	$5.5^{+2.4}_{-1.4}$	3.8 ± 0.4
A2631	0.273	1.26	$7.0^{+0.7}_{-0.5}$	19.5 ± 0.5	$6.9^{+0.8}_{-0.5}$	14.1 ± 0.5

curve cleaning was performed by hand to remove periods of high background that were not detected in the M08 analysis. This generally led to a small decrease in cluster temperature, consistent with the removal of a harder spectral component. For two clusters (RXJ1701+6414, RXJ1525+0958) the decrease was significant compared to the statistical uncertainties on kT (both decreased from ≈ 5 keV to ≈ 4 keV). For two other clusters the change in kT was large, but within the statistical uncertainties: CLJ0216-1747 decreased from ≈ 8 keV to ≈ 6 keV and CLJ1334+5031 decreased from ≈ 16 keV to ≈ 6 keV. For one cluster (CLJ1216+2633), the good time remaining after the new cleaning was too short for useful analysis, and this cluster was dropped from the sample, reducing the total number to 114 clusters. Finally, for AS1063, a redshift of 0.252 was erroneously used in M08, and this was corrected to 0.348 for the current analysis.

There have been several significant updates to the *Chandra* calibration since the analysis presented in M08, which was based on CALDB version 3.2.3. The most significant changes for the measurement of cluster temperatures and luminosities were updates to the mirror effective area, and the ACIS contamination model. Reese et al. (2010) recently examined the effect of *Chandra* calibration changes on the temperatures of galaxy clusters, finding that on average, temperatures measured with CALDB 3.1 were 6% higher than those measured with CALDB 4.2. The average temperature change (for kT measured within R_{500}) from M08 to the current analysis was $\langle kT_{old}/kT_{new} \rangle = 1.00 \pm 0.06$, where the uncertainty is the standard deviation of the clusters, and those clusters with significant individual changes discussed above were excluded. This is smaller than the change found by Reese et al. (2010), but we note that unlike that work, our study was not optimised to study the effect of calibration changes; there were numerous other changes between the M08 analysis and the current work, as discussed above.

The bolometric luminosities measured within R_{500} were also compared with M08, and the new luminosities were found to be higher by 8% on average ($\langle L_{X,old}/L_{X,new} \rangle = 0.93 \pm 0.06$). This is consistent with the $\approx 9\%$ decrease in the effective area at low energies introduced in CALDB 4.1.1¹.

We note that all of the main results in the following sections were also present with similar statistical significance in the data as presented in M08, so our results are not sensitive to the various calibration and analysis changes.

3 QUANTIFYING DYNAMICAL STATE AND COOL CORE PRESENCE

The dynamical state of the cluster was quantified by measuring the centroid shift, following the method of Poole et al. (2006). The centroid shift ($\langle w \rangle$) was defined as the standard deviation of the distance between the X-ray peak and centroid, with the latter measured in a series of circular apertures centred on the X-ray peak and decreasing in steps of 5% from R_{500} to $0.05R_{500}$. For some clusters, R_{500} extended beyond the edges of the detector in some directions. A maximum radius (R_w) within which $\langle w \rangle$ could be measured was

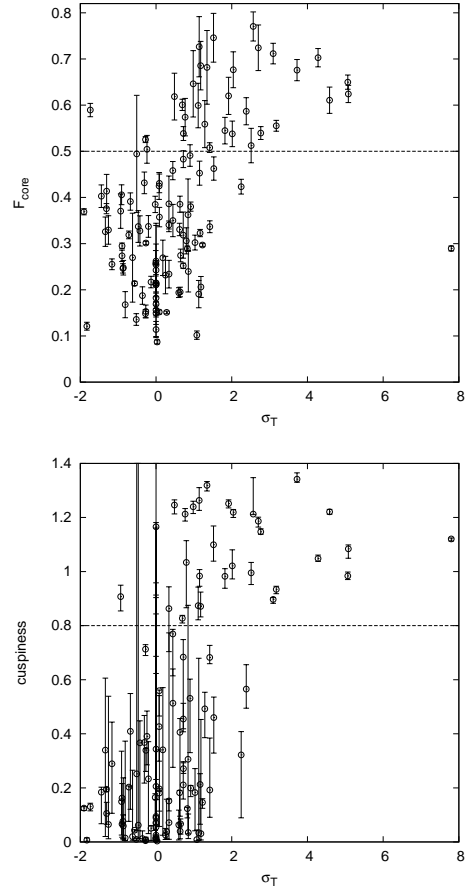


Figure 1. Comparison of simple cool core proxies F_{core} (top panel) and cuspsiness (bottom panel) with σ_T . The dashed horizontal line in each plot indicates the value of each property used to divide the sample into CC and NCC clusters. The outlier at $\sigma_T \approx 8$ is the merging, double cool core cluster A115.

thus defined for each cluster, such that the maximum fraction of the area within this radius that was lost to excluded regions, or off the edge of the detector was 2%. Following Poole et al. (2006), the central 30 kpc were excluded from these centroid measurements to increase the sensitivity to faint structure. In an improvement to M08, the uncertainties on the centroid shifts were calculated from Monte Carlo randomisations of the X-ray images, with the measurement of $\langle w \rangle$ being repeated for 100 realisations of the input image with pixels randomised under a Poisson distribution. This takes into account the effect of the image noise, while in M08, the error was derived simply from the number of values used in the standard deviation calculation.

In addition to quantifying cluster morphology with the centroid shift, two quantities were used to determine if a cluster was likely to host a cool core. In a recent comprehensive study, Hudson et al. (2010) tested 16 cool core probes, and concluded that for high quality data, a direct measurement of the central cooling time is preferred, but in lower quality data the cuspsiness of the gas density profile was recommended (see also Vikhlinin et al. 2006a). As our sample spans a wide range of redshift and L_X , cuspsiness is a more appropriate choice as it can be measured reliably for all clus-

¹ http://asc.harvard.edu/ciao/why/caldb4.1.1_hrma.html

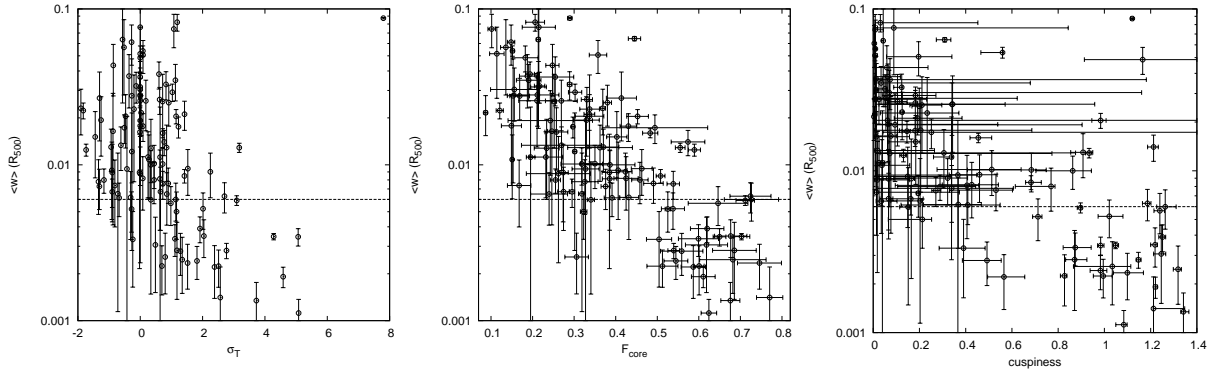


Figure 2. Comparison of cluster dynamical state with cool core proxy. The centroid shift is plotted against σ_T (left panel), F_{core} (centre panel) and cuspiness (right panel). The dashed line indicates the value of $\langle w \rangle = 0.006 R_{500}$ used to separate relaxed and unrelaxed clusters.

ters. Cuspiness is defined as the logarithmic slope of the gas density profile at a radius of $0.04 R_{500}$, and was measured using the best fitting gas density models, with the uncertainty derived from the cuspiness measured for each of the Monte Carlo randomisations of the density profile. The second quantity used was the core flux ratio (F_{core}), defined as the ratio of the bolometric unabsorbed flux from the central $0.15 R_{500}$ to the total within R_{500} . This quantity is the most robust to variations in the X-ray data quality and angular scale with redshift. F_{core} values were also computed using rest-frame (0.5 – 2) keV band unabsorbed fluxes, but this made no significant difference, so bolometric fluxes were used.

The most direct test of the presence of a cool core would be a temperature profile, but the data available are not sufficient for full temperature profiles for the majority of clusters in our sample. Instead, the projected temperature was measured for each cluster in a core (0 – $0.15 R_{500}$) aperture and outer ($0.15 - 0.3 R_{500}$) aperture, chosen to sample respectively the central dip and subsequent peak of the temperature profile of a typical cool core cluster (Vikhlinin et al. 2006b). The significance of the difference between the outer and core temperatures then gives a direct measurement of any cool core. This quantity (σ_T) was defined as the difference in temperatures divided by the quadrature sum of their measurement errors, such that positive σ_T indicates a cooler core region. This probe is sensitive to the data quality, and not just the strength of any cool core, so cool core clusters with low signal to noise observations could have $\sigma_T \approx 0$. However, large values of σ_T are an unambiguous indicator of cool core presence and can be used to calibrate other cool core proxies which are less sensitive to data quality. The dynamical properties of the clusters are given in Table 2.

Figure 1 shows the cool core proxies plotted against σ_T , and these plots were used to define the value of each proxy used to split the sample into clusters with and without cool cores (referred to as CC and NCC clusters hereafter). Almost all clusters with $\sigma_T \gtrsim 2$ have $F_{\text{core}} > 0.5$ (i.e. more than half of the flux within R_{500} comes from the central 15%), and we thus define $F_{\text{core}} = 0.5$ as the border between CC and NCC clusters in the F_{core} parameter space, giving 31 CC and 83 NCC clusters. Similarly, almost all clusters with $\sigma_T \gtrsim 2$ have cuspiness > 0.8 , so this is defined as the CC/NCC boundary in cuspiness, giving 30 CC and 84 NCC clusters

(this is similar to the value of 0.7 adopted to define strong cool cores in Vikhlinin et al. 2006a).

There is substantial overlap between the subsamples defined in F_{core} and cuspiness, and unless specified otherwise, in the following sections all results are shown for the CC/NCC populations defined by F_{core} .

The dynamical state of the clusters is also related to their cool core status in the sense that cool core clusters tend to be dynamically relaxed. This is illustrated in figure 2 which shows the centroid shift parameter plotted against each of the cool core measures. The most relaxed clusters show evidence for cool cores in all of the different measures (albeit with a larger dispersion for cuspiness), and we adopt a threshold of $\langle w \rangle = 0.006 R_{500}$ below which clusters are classed as “relaxed” (28 clusters), and above which as “unrelaxed” (86 clusters). This a minor update to the value of $\langle w \rangle = 0.005 R_{500}$ used to segregate the clusters in Maughan (2007).

We finally define a split into 21 clusters that passed the combined filter of all three of the above tests ($F_{\text{core}} > 0.5$, cuspiness > 0.8 , $\langle w \rangle > 0.006 R_{500}$), and 93 clusters that do not. These clusters that are both relaxed and pass both cool core filters are referred to as RCC clusters (for “relaxed cool core clusters”), while the complementary set are referred to as NRCC clusters.

4 STRONG SELF-SIMILARITY

The strong self-similarity of the $L_X - kT$ relation of the population was investigated. Figure 3 shows the $L_X - kT$ relation where both quantities were measured within R_{500} , including the core regions. A power law of the form

$$L_X = E(z) A_{LT} (kT/T_*)^{B_{LT}}, \quad (3)$$

was fit to the data, with T_* set at 6 keV (close to the median temperature of 5.9 keV for the full sample). The model was fit in log space using BCES orthogonal regression (Akritas & Bershady 1996), and the intrinsic scatter about the best fitting model was estimated by adding an extra error term in quadrature to every data point until the reduced χ^2 was unity (see Maughan 2007, for details). The intrinsic scatter of a population is thus measured in the L_X direction about the best fitting $L_X - kT$ relation for that

Table 2: Summary of the cluster dynamical properties. σ_T indicates the significance of the temperature decrease in the core region, F_{core} is the ratio of the bolometric flux within $0.15R_{500}$ to that within R_{500} , cuspiness is the logarithmic slope of the gas density profile at $0.04R_{500}$, and $\langle w \rangle$ is the centroid shift, with R_w giving the maximum radius within which $\langle w \rangle$ could be measured.

Cluster	σ_T	F_{core}	cuspiness	$\langle w \rangle (10^{-3} R_{500})$	$R_w (R_{500})$
MS0015.9+1609	-0.9	0.298 ± 0.006	$0.162^{+0.054}_{-0.095}$	6.7 ± 1.4	1.00
RXJ0027.6+2616	-0.0	0.240 ± 0.028	$0.013^{+0.144}_{-0.008}$	16.2 ± 7.0	1.00
CLJ0030+2618	0.0	0.262 ± 0.081	$0.018^{+0.138}_{-0.011}$	8.8 ± 6.4	1.00
A68	-0.9	0.410 ± 0.022	$0.149^{+0.186}_{-0.123}$	9.2 ± 4.8	1.00
A115	7.8	0.292 ± 0.005	$1.121^{+0.004}_{-0.008}$	87.2 ± 0.9	1.00
A209	1.2	0.321 ± 0.008	$0.213^{+0.040}_{-0.147}$	5.0 ± 1.7	0.95
CLJ0152.7-1357S	1.2	0.212 ± 0.022	$0.031^{+0.422}_{-0.024}$	82.2 ± 10.2	1.00
A267	-1.3	0.415 ± 0.036	$0.105^{+0.041}_{-0.040}$	26.8 ± 12.6	1.00
CLJ0152.7-1357N	-0.4	0.192 ± 0.018	$0.012^{+0.029}_{-0.009}$	37.0 ± 13.9	1.00
MACSJ0159.8-0849	2.8	0.547 ± 0.014	$1.147^{+0.011}_{-0.010}$	2.8 ± 0.3	1.00
CLJ0216-1747	0.0	0.255 ± 0.038	$0.073^{+1.109}_{-0.068}$	36.6 ± 12.7	1.00
RXJ0232.2-4420	1.1	0.455 ± 0.027	$0.984^{+0.024}_{-0.038}$	20.4 ± 2.2	1.00
MACSJ0242.5-2132	1.1	0.726 ± 0.065	$1.263^{+0.047}_{-0.037}$	6.0 ± 1.6	1.00
A383	4.6	0.616 ± 0.029	$1.221^{+0.009}_{-0.009}$	1.9 ± 0.3	1.00
MACSJ0257.6-2209	0.9	0.496 ± 0.024	$0.531^{+0.071}_{-0.201}$	7.6 ± 1.9	1.00
MS0302.7+1658	-0.5	0.487 ± 0.124	$0.252^{+3.511}_{-0.209}$	17.3 ± 3.6	1.00
CLJ0318-0302	-0.5	0.339 ± 0.034	$0.062^{+3.450}_{-0.049}$	20.5 ± 7.7	1.00
MACSJ0329.6-0211	0.8	0.593 ± 0.042	$1.213^{+0.020}_{-0.026}$	14.0 ± 2.6	1.00
MACSJ0404.6+1109	0.6	0.194 ± 0.011	$0.063^{+0.054}_{-0.056}$	38.2 ± 7.5	1.00
MACSJ0429.6-0253	1.9	0.621 ± 0.040	$1.252^{+0.014}_{-0.016}$	3.9 ± 0.7	1.00
RXJ0439.0+0715	0.4	0.460 ± 0.020	$0.769^{+0.017}_{-0.155}$	8.0 ± 2.4	1.00
RXJ0439+0520	1.0	0.648 ± 0.073	$1.240^{+0.020}_{-0.025}$	5.7 ± 1.6	1.00
MACSJ0451.9+0006	-1.3	0.345 ± 0.030	$0.065^{+0.474}_{-0.053}$	19.3 ± 8.0	1.00
A521	0.1	0.154 ± 0.004	$0.559^{+0.003}_{-0.094}$	53.8 ± 4.1	1.00
A520	-0.6	0.213 ± 0.005	$0.043^{+0.002}_{-0.006}$	63.6 ± 38.7	1.00
MS0451.6-0305	-0.2	0.332 ± 0.023	$0.233^{+0.137}_{-0.203}$	22.7 ± 15.0	1.00
CLJ0522-3625	0.3	0.253 ± 0.033	$0.071^{+0.702}_{-0.062}$	12.8 ± 6.8	1.00
CLJ0542.8-4100	-0.9	0.242 ± 0.016	$0.059^{+0.178}_{-0.051}$	43.4 ± 15.8	1.00
MACSJ0647.7+7015	-0.3	0.437 ± 0.021	$0.368^{+0.100}_{-0.150}$	6.2 ± 2.9	1.00
1E0657-56	1.2	0.301 ± 0.004	$0.146^{+0.014}_{-0.022}$	17.5 ± 2.7	1.00
MACSJ0717.5+3745	0.7	0.256 ± 0.006	$0.211^{+0.086}_{-0.052}$	25.5 ± 12.6	1.00
A586	-0.2	0.502 ± 0.030	$0.391^{+0.093}_{-0.106}$	3.3 ± 1.7	0.75
MACSJ0744.9+3927	0.7	0.487 ± 0.019	$0.455^{+0.058}_{-0.036}$	16.0 ± 1.1	1.00
A665	0.8	0.288 ± 0.005	$0.123^{+0.005}_{-0.034}$	32.8 ± 6.8	0.75
A697	0.3	0.347 ± 0.009	$0.151^{+0.008}_{-0.037}$	6.0 ± 4.5	0.95
CLJ0848.7+4456	0.0	0.212 ± 0.057	$0.055^{+0.568}_{-0.047}$	28.0 ± 10.4	1.00
ZWCLJ1953	0.1	0.433 ± 0.020	$0.181^{+0.015}_{-0.067}$	17.7 ± 3.6	1.00
CLJ0853+5759	0.0	0.120 ± 0.022	$0.008^{+0.010}_{-0.004}$	51.6 ± 24.9	1.00
MS0906.5+1110	-2.3	0.443 ± 0.015	$0.309^{+0.027}_{-0.036}$	64.5 ± 2.0	0.90
RXJ0910+5422	0.0	0.196 ± 0.042	$0.343^{+0.615}_{-0.333}$	25.8 ± 12.8	1.00
A773	-1.3	0.378 ± 0.011	$0.195^{+0.006}_{-0.008}$	7.3 ± 2.1	1.00
A781	-0.3	0.154 ± 0.009	$0.005^{+0.004}_{-0.002}$	61.2 ± 17.7	1.00
CLJ0926+1242	0.8	0.303 ± 0.032	$1.034^{+0.080}_{-0.168}$	2.6 ± 1.1	1.00
RBS797	1.5	0.743 ± 0.054	$1.099^{+0.069}_{-0.061}$	2.3 ± 0.7	1.00
MACSJ0949.8+1708	0.6	0.393 ± 0.018	$0.406^{+0.051}_{-0.310}$	8.1 ± 4.3	1.00
CLJ0956+4107	0.0	0.219 ± 0.020	$0.013^{+0.006}_{-0.006}$	31.6 ± 14.5	1.00
A907	3.2	0.555 ± 0.012	$0.934^{+0.012}_{-0.016}$	12.9 ± 0.9	0.95
MS1006.0+1202	1.4	0.340 ± 0.013	$0.192^{+0.192}_{-0.101}$	21.1 ± 4.5	1.00
MS1008.1-1224	0.1	0.358 ± 0.021	$0.196^{+0.144}_{-0.139}$	50.6 ± 12.1	1.00
ZW3146	5.1	0.654 ± 0.016	$0.984^{+0.014}_{-0.013}$	3.5 ± 0.4	1.00
CLJ1113.1-2615	0.8	0.355 ± 0.077	$0.306^{+0.570}_{-0.276}$	12.9 ± 5.1	1.00
A1204	2.7	0.727 ± 0.051	$1.186^{+0.015}_{-0.022}$	6.3 ± 1.4	1.00
CLJ1117+1745	0.0	0.134 ± 0.028	$0.205^{+0.481}_{-0.199}$	17.8 ± 10.4	1.00
CLJ1120+4318	-0.4	0.352 ± 0.036	$0.366^{+0.082}_{-0.354}$	9.4 ± 11.0	1.00
RXJ1121+2327	-0.5	0.146 ± 0.013	$0.009^{+0.006}_{-0.004}$	56.7 ± 28.6	1.00

continued on next page

Table 2: *continued*

Cluster	σ_T	F_{core}	cuspsiness	$\langle w \rangle (10^{-3} R_{500})$	$R_w (R_{500})$
A1240	0.0	0.091 ± 0.005	$0.003^{+0.001}_{-0.001}$	21.6 ± 6.2	1.00
MACSJ1131.8-1955	1.0	0.306 ± 0.016	$0.183^{+0.088}_{-0.142}$	29.2 ± 3.7	1.00
MS1137.5+6625	0.1	0.435 ± 0.030	$0.426^{+0.115}_{-0.128}$	8.2 ± 3.1	1.00
MACSJ1149.5+2223	-0.9	0.251 ± 0.010	$0.076^{+0.024}_{-0.064}$	16.4 ± 12.3	1.00
A1413	-0.3	0.498 ± 0.006	$0.713^{+0.017}_{-0.023}$	5.2 ± 1.5	0.85
CLJ1213+0253	0.0	0.258 ± 0.118	$0.094^{+0.809}_{-0.082}$	19.2 ± 10.7	1.00
RXJ1221+4918	0.6	0.195 ± 0.010	$0.040^{+0.030}_{-0.028}$	11.2 ± 12.3	1.00
CLJ1226.9+3332	1.5	0.459 ± 0.028	$0.460^{+0.076}_{-0.132}$	9.5 ± 3.1	1.00
RXJ1234.2+0947	1.1	0.110 ± 0.009	$0.009^{+0.036}_{-0.005}$	74.3 ± 18.0	1.00
RDCS1252-29	-0.8	0.168 ± 0.029	$0.014^{+0.359}_{-0.009}$	7.4 ± 3.4	1.00
A1682	0.2	0.222 ± 0.039	$0.026^{+0.024}_{-0.017}$	11.2 ± 5.1	0.80
MACSJ1311.0-0310	2.4	0.594 ± 0.029	$0.565^{+0.090}_{-0.071}$	2.2 ± 0.8	1.00
A1689	0.7	0.600 ± 0.012	$0.827^{+0.010}_{-0.018}$	2.2 ± 0.8	1.00
RXJ1317.4+2911	0.0	0.174 ± 0.120	$0.069^{+1.092}_{-0.066}$	30.4 ± 11.4	1.00
CLJ1334+5031	0.0	0.226 ± 0.040	$0.089^{+0.754}_{-0.070}$	76.3 ± 37.2	1.00
A1763	-0.7	0.319 ± 0.008	$0.203^{+0.005}_{-0.127}$	6.5 ± 5.4	0.90
RXJ1347.5-1145	3.1	0.717 ± 0.023	$0.897^{+0.007}_{-0.014}$	5.9 ± 0.4	1.00
RXJ1350.0+6007	1.1	0.161 ± 0.024	$0.034^{+0.646}_{-0.028}$	34.9 ± 9.2	1.00
CLJ1354-0221	0.0	0.157 ± 0.021	$0.025^{+0.206}_{-0.018}$	27.6 ± 8.2	1.00
CLJ1415.1+3612	-0.9	0.369 ± 0.038	$0.907^{+0.042}_{-0.053}$	13.0 ± 3.9	1.00
RXJ1416+4446	0.3	0.394 ± 0.061	$0.863^{+0.081}_{-0.159}$	10.0 ± 2.3	1.00
MACSJ1423.8+2404	0.5	0.621 ± 0.051	$1.246^{+0.019}_{-0.033}$	3.1 ± 1.5	1.00
A1914	-1.7	0.592 ± 0.015	$0.131^{+0.013}_{-0.016}$	12.5 ± 1.1	0.65
A1942	-1.2	0.256 ± 0.012	$0.289^{+0.154}_{-0.183}$	8.0 ± 1.4	1.00
MS1455.0+2232	4.3	0.709 ± 0.020	$1.048^{+0.013}_{-0.011}$	3.5 ± 0.2	1.00
RXJ1504-0248	2.6	0.774 ± 0.037	$1.212^{+0.135}_{-0.002}$	1.4 ± 0.8	1.00
A2034	-0.3	0.302 ± 0.004	$0.339^{+0.006}_{-0.078}$	12.2 ± 9.3	0.75
A2069	0.3	0.147 ± 0.003	$0.038^{+0.120}_{-0.026}$	10.8 ± 4.8	0.75
RXJ1525+0958	-0.3	0.162 ± 0.015	$0.008^{+0.009}_{-0.004}$	27.7 ± 20.1	1.00
RXJ1532.9+3021	1.2	0.691 ± 0.054	$0.871^{+0.053}_{-0.039}$	2.8 ± 1.5	1.00
A2111	0.6	0.274 ± 0.014	$0.067^{+0.019}_{-0.038}$	6.7 ± 2.9	1.00
A2125	-1.8	0.125 ± 0.009	$0.007^{+0.008}_{-0.005}$	22.3 ± 2.6	1.00
A2163	0.9	0.376 ± 0.010	$0.199^{+0.010}_{-0.032}$	25.0 ± 7.4	0.60
MACSJ1621.3+3810	2.5	0.538 ± 0.038	$0.995^{+0.039}_{-0.043}$	2.2 ± 0.6	1.00
MS1621.5+2640	-0.1	0.226 ± 0.013	$0.051^{+0.009}_{-0.045}$	32.1 ± 7.2	1.00
A2204	3.7	0.681 ± 0.023	$1.342^{+0.024}_{-0.011}$	1.3 ± 0.4	0.75
A2218	-1.9	0.373 ± 0.007	$0.125^{+0.005}_{-0.009}$	23.0 ± 7.5	1.00
CLJ1641+4001	0.9	0.261 ± 0.051	$0.035^{+0.068}_{-0.022}$	6.5 ± 2.4	1.00
RXJ1701+6414	0.7	0.328 ± 0.052	$0.684^{+0.064}_{-0.276}$	10.1 ± 2.7	1.00
RXJ1716.9+6708	-1.3	0.335 ± 0.033	$0.340^{+0.267}_{-0.319}$	7.8 ± 3.0	1.00
A2259	-0.0	0.394 ± 0.018	$0.165^{+0.014}_{-0.122}$	8.9 ± 6.8	0.85
RXJ1720.1+2638	5.1	0.625 ± 0.018	$1.084^{+0.014}_{-0.035}$	1.1 ± 0.3	1.00
MACSJ1720.2+3536	1.8	0.552 ± 0.029	$0.983^{+0.028}_{-0.044}$	2.4 ± 0.6	1.00
A2261	1.4	0.509 ± 0.011	$0.682^{+0.044}_{-0.023}$	8.5 ± 0.8	1.00
A2294	-0.7	0.388 ± 0.019	$0.409^{+0.140}_{-0.289}$	6.1 ± 1.5	0.65
MACSJ1824.3+4309	0.0	0.210 ± 0.036	$1.166^{+0.246}_{-0.252}$	48.6 ± 9.2	1.00
MACSJ1931.8-2634	2.0	0.686 ± 0.040	$1.219^{+0.010}_{-0.019}$	3.5 ± 0.9	1.00
RXJ2011.3-5725	1.3	0.561 ± 0.051	$0.492^{+0.062}_{-0.107}$	2.8 ± 0.8	1.00
MS2053.7-0449	0.4	0.354 ± 0.035	$0.513^{+0.127}_{-0.237}$	10.2 ± 3.1	1.00
MACSJ2129.4-0741	-1.4	0.401 ± 0.024	$0.184^{+0.018}_{-0.117}$	15.1 ± 6.9	1.00
RXJ2129.6+0005	2.0	0.544 ± 0.028	$1.021^{+0.059}_{-0.048}$	5.2 ± 1.4	1.00
A2409	2.3	0.418 ± 0.016	$0.322^{+0.086}_{-0.233}$	9.0 ± 2.9	0.65
MACSJ2228.5+2036	0.6	0.335 ± 0.014	$0.182^{+0.008}_{-0.130}$	26.2 ± 5.2	1.00
MACSJ2229.7-2755	1.3	0.686 ± 0.082	$1.319^{+0.014}_{-0.021}$	2.5 ± 1.0	1.00
MACSJ2245.0+2637	1.1	0.603 ± 0.050	$0.874^{+0.069}_{-0.052}$	3.4 ± 0.8	1.00
RXJ2247+0337	-0.6	0.284 ± 0.100	$0.020^{+0.245}_{-0.013}$	13.3 ± 4.2	1.00
AS1063	0.7	0.549 ± 0.016	$0.271^{+0.022}_{-0.017}$	7.5 ± 1.5	1.00
CLJ2302.8+0844	0.2	0.281 ± 0.038	$0.341^{+0.230}_{-0.316}$	25.7 ± 9.2	1.00
A2631	-0.9	0.276 ± 0.012	$0.066^{+0.088}_{-0.049}$	8.9 ± 4.6	1.00

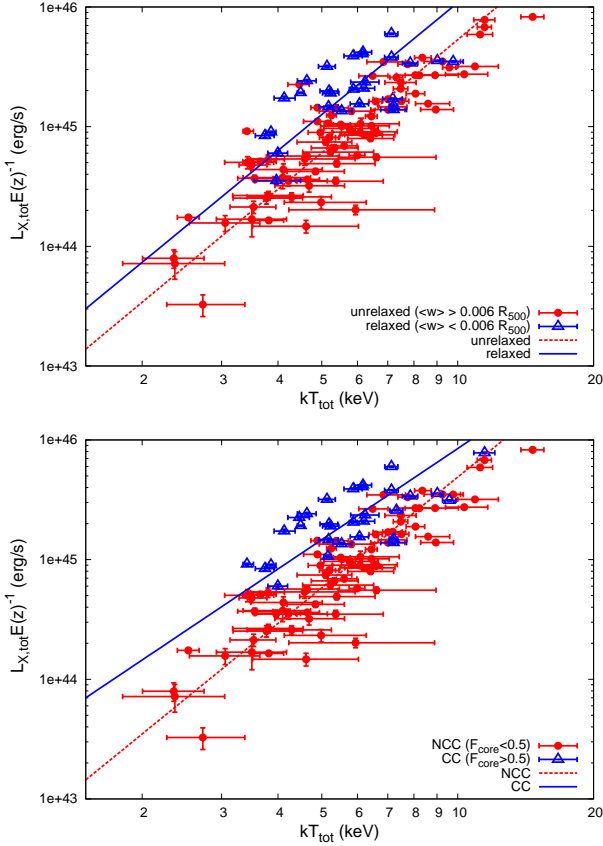


Figure 3. $L_X - kT$ relation for the cluster sample, separated into relaxed/unrelaxed subsamples (top panel) or CC/NCC subsamples (bottom panel). L_X and kT were measured within R_{500} , including the core regions. Luminosities are corrected for self-similar evolution as indicated on the ordinate axis. The lines show the best fitting power laws determined from a BCES orthogonal regression fit (see text for details).

population, and is denoted as $\sigma_{L|T}$.

The $L_X - kT$ relation was fit for the full cluster population, and the CC/NCC and relaxed/unrelaxed subsets, and the best fitting parameters and measured intrinsic dispersion are given in Table 3. In all cases, the normalisation measured for the CC or relaxed clusters was significantly higher than that of the NCC or unrelaxed clusters. This is in line with expectations, and the effect is clear in the distribution of the clusters in the $L_X - kT$ plane. The intrinsic scatter of each of the relaxed/CC subsamples is larger than the unrelaxed/NCC subsamples, and the highest scatter is that of the population as a whole. This is consistent with the relaxed/CC clusters and unrelaxed/NCC clusters forming two fairly distinct populations, offset in the $L_X - kT$ plane.

In order to remove the strong effect of the cool cores, the $L_X - kT$ relation was also derived for core-excised cluster properties (i.e. both L_X and kT measured in the $[0.15 - 1]R_{500}$ aperture). The resulting $L_X - kT$ relations are plotted in Figure 4, again for the whole population, and for relaxed/unrelaxed and CC/NCC subsets. The relations were fit as before and the best fitting parameters are given in Table 4. In these core-excised relations, the $L_X - kT$ normalisations for all subsamples and the overall population

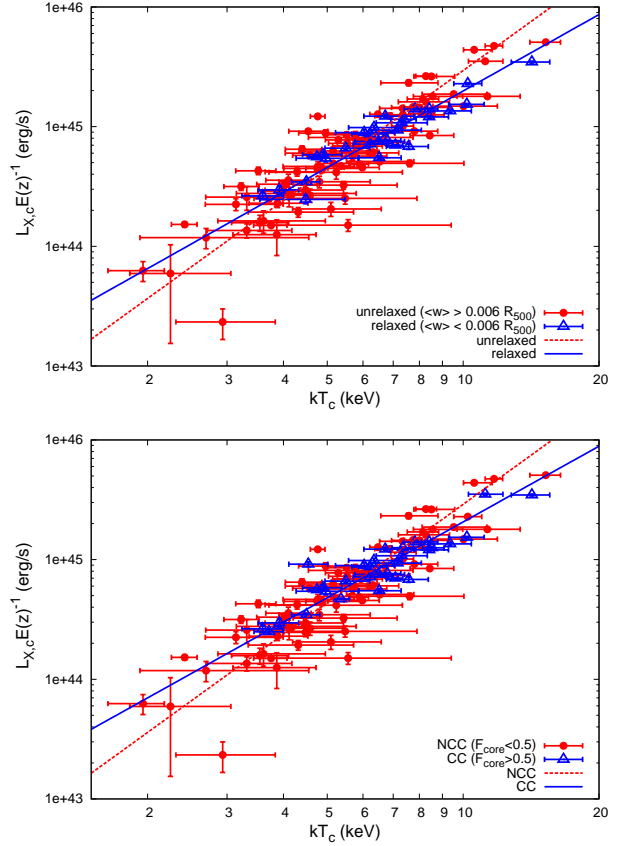


Figure 4. $L_X - kT$ relation for the cluster sample, separated into relaxed/unrelaxed subsamples (top panel) or CC/NCC subsamples (bottom panel). L_X and kT were measured within R_{500} , with the central $0.15R_{500}$ excluded. Luminosities are corrected for self-similar evolution as indicated on the ordinate axis. The lines show the best fitting power laws determined from a BCES orthogonal regression fit (see text for details).

are in good agreement, indicating that the core excision has removed the offset between the relaxed/CC and unrelaxed/NCC populations.

In common with previous studies of luminosity scaling relations (e.g. Markevitch 1998; Maughan 2007; Pratt et al. 2009), the intrinsic scatter of the whole population was significantly reduced by the exclusion of the cores, from 67% to 30% in this case. Indeed, the intrinsic scatter of each of the subsamples was reduced. The typical reduction in dispersion for the unrelaxed/NCC clusters was from $\sim 40\%$ to $\sim 30\%$, while for the relaxed/CC clusters the effect was stronger, with a typical reduction from $\sim 50\%$ to $\sim 15\%$ (albeit with larger uncertainties on the intrinsic scatter). Also of note is that the 21 RCC clusters (corresponding to the most relaxed clusters with strongest cool cores) have no measurable intrinsic scatter when the cores are removed, indicating a very regular population. The core-excised $L_X - kT$ relation for subsamples separated by the combined filter (RCC and NRCC) is shown in Fig. 5.

The removal of the core regions also has the effect of reducing the slope of the $L_X - kT$ relation for each subsample, although the effect is not always significant. The strongest effect is for the population fit as a whole, and is most likely due to the offset $L_X - kT$ relations of the CC and NCC

category	filter	N	A_{LT} (10^{44} erg s $^{-1}$)	B_{LT}	σ_{LT} (%)
all	none	114	12.94 ± 1.00	3.63 ± 0.27	67.2 ± 4.8
CC	cuspiness ≥ 0.8	30	26.30 ± 3.68	3.33 ± 0.60	54.6 ± 4.6
NCC	cuspiness < 0.8	84	9.75 ± 0.55	3.18 ± 0.20	36.8 ± 4.4
CC	$F_{core} \geq 0.5$	31	23.28 ± 2.27	2.53 ± 0.44	50.6 ± 5.6
NCC	$F_{core} < 0.5$	83	10.02 ± 0.56	3.19 ± 0.20	38.1 ± 4.4
relaxed	$\langle w \rangle \leq 0.006$	28	22.23 ± 2.98	3.10 ± 0.61	61.1 ± 6.1
unrelaxed	$\langle w \rangle > 0.006$	86	10.54 ± 0.70	3.26 ± 0.22	48.5 ± 6.9
RCC	combined	21	27.35 ± 2.64	2.44 ± 0.43	38.0 ± 3.2
NRCC	combined	93	10.57 ± 0.64	3.22 ± 0.20	46.9 ± 6.0

Table 3. $L_X - kT$ relations for properties measured with core regions included ($[0-1]R_{500}$ aperture). The first column gives the category of each subsample, and the second column gives the filter used to define that subsample. The combined filter refers to clusters with cuspiness > 0.8 , $F_{core} > 0.5$, and $\langle w \rangle < 0.006$. The third column gives the number of clusters in each subsample. The fourth, fifth and sixth columns give the normalisation and slope of the best fitting model and the intrinsic scatter of the data about that model. The model used was $L_X = E(z)A_{LT}(kT/T_*)^{B_{LT}}$, with $T_* = 6$ keV in all cases.

category	filter	N	A_{LT} (10^{44} erg s $^{-1}$)	B_{LT}	σ_{LT} (%)
all	none	114	6.98 ± 0.30	2.72 ± 0.18	29.7 ± 4.2
CC	cuspiness ≥ 0.8	30	7.16 ± 0.33	2.15 ± 0.17	13.0 ± 11.7
NCC	cuspiness < 0.8	84	6.98 ± 0.39	2.82 ± 0.21	33.1 ± 5.3
CC	$F_{core} \geq 0.5$	31	7.05 ± 0.34	2.10 ± 0.13	19.2 ± 5.1
NCC	$F_{core} < 0.5$	83	7.18 ± 0.38	2.86 ± 0.22	31.4 ± 6.2
relaxed	$\langle w \rangle \leq 0.006$	28	6.71 ± 0.34	2.12 ± 0.17	12.5 ± 6.5
unrelaxed	$\langle w \rangle > 0.006$	86	7.28 ± 0.39	2.86 ± 0.21	32.4 ± 5.9
RCC	combined	21	7.28 ± 0.26	1.90 ± 0.14	1.8 ± 3.1
NRCC	combined	93	7.10 ± 0.36	2.82 ± 0.19	32.5 ± 5.1

Table 4. $L_X - kT$ relations for properties measured with core regions excluded ($[0.15-1]R_{500}$ aperture). The first column gives the category of each subsample, and the second column gives the filter used to define that subsample. The combined filter refers to clusters with cuspiness > 0.8 , $F_{core} > 0.5$, and $\langle w \rangle < 0.006$. The third column gives the number of clusters in each subsample. The fourth, fifth and sixth columns give the normalisation and slope of the best fitting model and the intrinsic scatter of the data about that model. The model used was $L_X = E(z)A_{LT}(kT/T_*)^{B_{LT}}$, with $T_* = 6$ keV in all cases.

clusters, combined with different distributions with temperature of the CC and NCC clusters. Specifically, the CC clusters which are offset above the rest of the population in the $L_X - kT$ plane are generally hotter in our sample (the median core-excised kT is 6.5 keV for CCs and 5.5 keV for NCCs). When the cores are excised, these clusters move significantly towards lower L_X and higher kT , giving rise to the flatter slope than when cores are not excised.

Perhaps of greater interest is that with cores excised, a difference in $L_X - kT$ slope is apparent between the relaxed/CC and unrelaxed/NCC populations. In all cases, the best fitting slope to the relaxed/CC clusters is shallower than that of the complementary population (see Fig. 5). The significance of the difference ranges from $\approx 2.5\sigma$ to $\approx 4\sigma$, with the strongest difference found for the populations split by the combined filter. It is striking that all of the relaxed/CC subsamples have $L_X - kT$ slopes consistent with the self-similar prediction of 2. This is a first indication that this part of the cluster population obeys self-similar scaling laws. This was investigated further via an examination of the cluster gas density profiles.

4.1 Similarity of gas density profiles

In order to investigate the apparent self-similarity of the $L_X - kT$ relation for the relaxed/CC clusters, the structure

of the gas density profiles were examined. The best fitting gas density models for each cluster were scaled by dividing the radial coordinate by R_{500} , and dividing the densities by $E^2(z)$ to remove the expected self-similar evolution (see e.g. Croston et al. 2008, for examples of the effects of these scalings). After these scalings, self-similar profiles would be identical. The scaled profiles are plotted in Figure 6, with the relaxed and unrelaxed clusters indicated. In both cases, the dispersion of the profiles is largest in the central regions, reducing at larger radii. For both subsamples, the dispersion in the profiles was significantly larger when the $E^2(z)$ scaling was not applied. It is apparent that the two subgroups have different gas density structures, with the relaxed clusters more centrally concentrated, and the unrelaxed clusters more diffuse.

These results demonstrate a lack of similarity between the gas density profiles of clusters selected as relaxed and unrelaxed. Next, the degree of self similarity within those subgroups was investigated. Figure 7 shows the scaled gas density profiles of the relaxed and unrelaxed clusters, colour-coded by system temperature (measured with the core excised). For the unrelaxed clusters, there is evidence for a temperature dependence of the profiles, with cooler systems tending to have lower densities than hotter systems at a given radius. For the relaxed clusters, no such trend is apparent. The temperature dependence of the density profiles

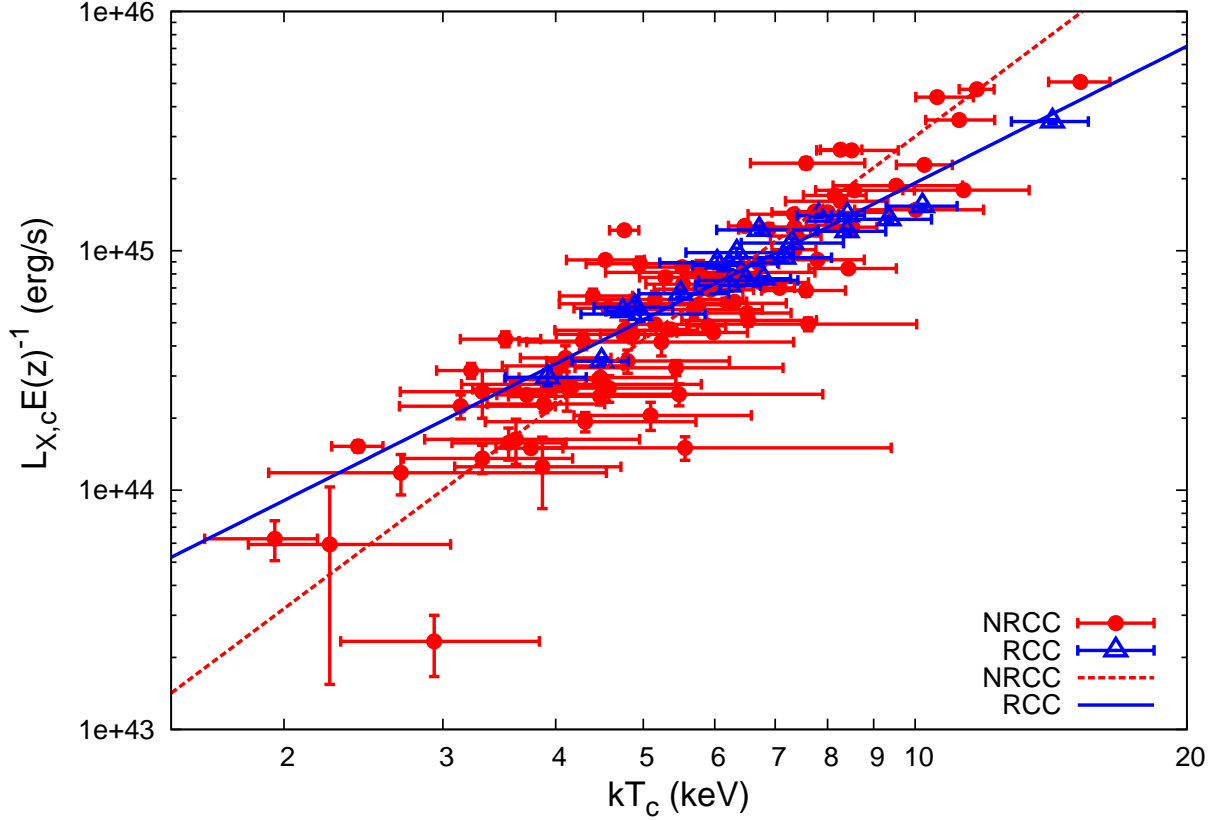


Figure 5. $L_X - kT$ relation for the cluster sample, split using our combined filter into a subsample containing the most relaxed clusters with strongest cool cores (RCC), and the complementary subsample (NRCC). L_X and kT were measured within R_{500} , with the central $0.15R_{500}$ excluded. Luminosities are corrected for self-similar evolution as indicated on the ordinate axis. The lines show the best fitting power laws determined from a BCES orthogonal regression fit (see text for details).

was examined in more detail by measuring the scaled density of each cluster at a fixed fraction of R_{500} , and plotting them against system temperature. An example plot for densities measured at $0.3R_{500}$ is shown in Figure 8. Despite the different temperature distributions of the two populations, the unrelaxed clusters clearly have a stronger dependence of gas density on temperature than the relaxed clusters.

The data for each subsample were then fit with a power law of the form:

$$\rho(r/R_{500})E^{-2}(z) = (kT)^\eta, \quad (4)$$

where we refer to η as the “similarity index” of the density profiles ($\eta = 0$ corresponds to self-similar profiles). This procedure was repeated at different values of r to produce the similarity index profile shown in Figure 9. The similarity index profile shows that the gas density profiles of the unrelaxed clusters have a strong temperature dependence in the core regions that becomes weaker with radius, approaching self-similarity by $\sim 0.7R_{500}$. A similar trend of decreasing similarity index with radius was observed by Croston et al. (2008) who found values of 0.5 and 0.25 at $0.3R_{500}$ and $0.7R_{500}$ respectively for their representative sample of clusters.

In contrast, the similarity index profile of the relaxed clusters is quite flat, with no strong dependence on temperature at any radius. As a test of the sensitivity of this dif-

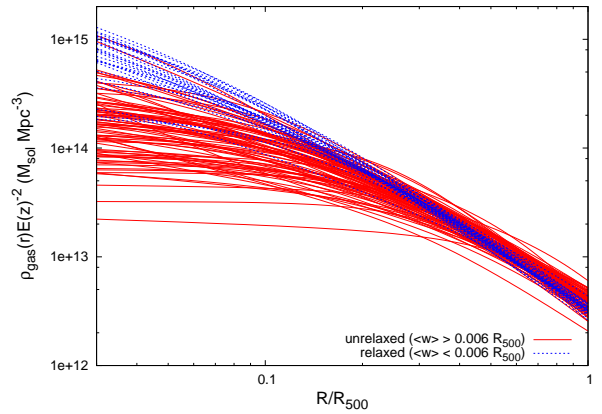


Figure 6. Scaled gas density profiles of the cluster sample. The profiles are the best fitting models to the observed cluster emissivity profiles (see text for details), and are scaled in radius by R_{500} and in density by $E^2(z)$. The solid lines indicate the unrelaxed clusters while the dashed lines are the profiles of the relaxed clusters.

ference in similarity index to the absence of relaxed clusters with low temperatures, unrelaxed clusters with $kT < 3.5$ keV were excluded from the fits. This made no significant difference to the slopes.

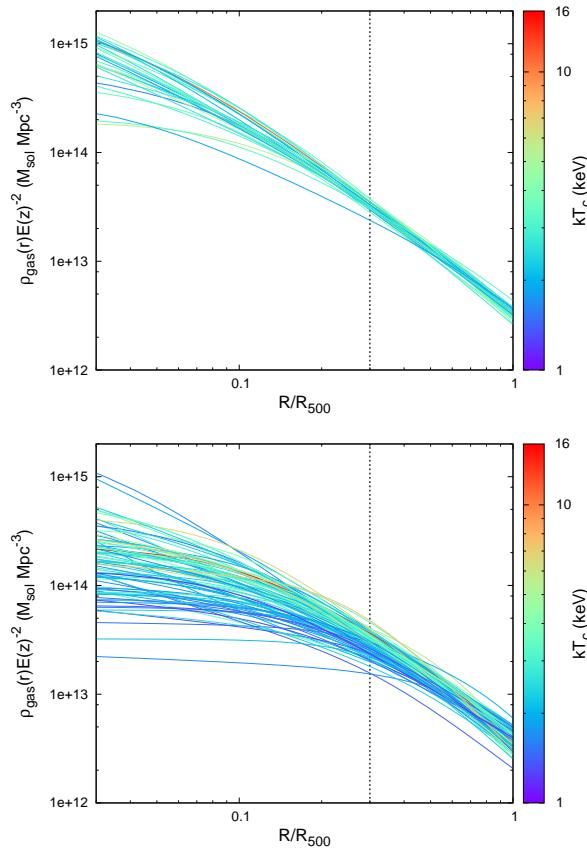


Figure 7. Scaled gas density profiles of the clusters, colour coded by system temperature (as measured in the $[0.15 - 1]R_{500}$ aperture). The top panel plots the relaxed clusters and the bottom panel plots the unrelaxed clusters.

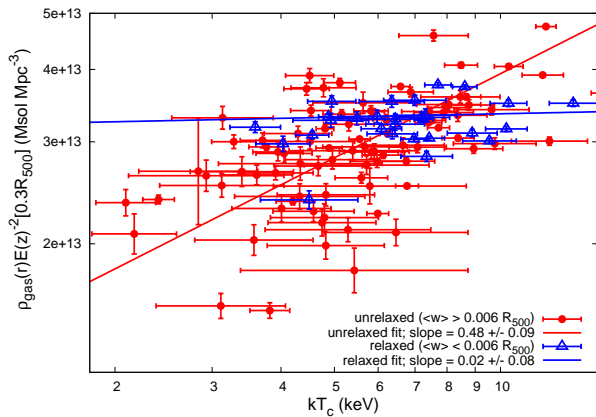


Figure 8. Scaled gas density at $0.3R_{500}$ is plotted against system temperature (as measured in the $[0.15 - 1]R_{500}$ aperture). Filled circles and hollow triangles indicate the unrelaxed and relaxed clusters respectively.

Very similar results were found for density profiles when the CC and NCC samples were compared, although we consider the separation on $\langle w \rangle$ to be preferable as this is less directly linked to the radial structure of the gas density than either the F_{core} or cuspiness measurements.

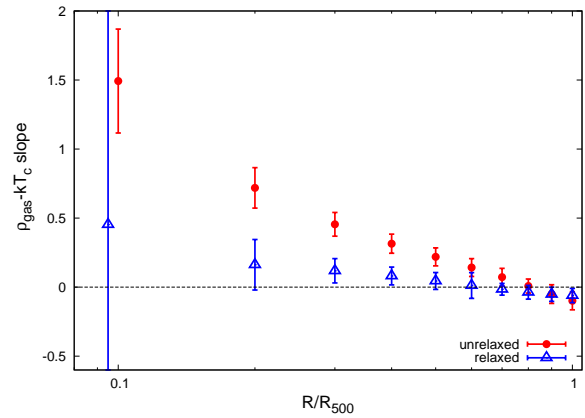


Figure 9. Similarity index (the slope of the power law dependence of scaled gas density on system temperature) is plotted as a function of scaled radius. Filled circles and hollow triangles indicate the unrelaxed and relaxed clusters respectively. The innermost points are slightly offset in radius for clarity.

5 EVOLUTION OF THE $L_X - kT$ RELATION

Thus far, it has been assumed that the redshift evolution of the $L_X - kT$ relation is self-similar, *i.e.* the slope is independent of redshift, while the normalisation increases with increasing redshift due to the increasing density of the clusters. As discussed in the introduction, there is some debate in the literature as to whether this evolution model is a good description of observed clusters, with evidence that selection biases play a significant role in evolution studies.

To investigate this further, the evolution in the $L_X - kT$ relation of the current *Chandra* cluster sample was examined. In order to measure evolution, a low redshift baseline must be defined. While many exist in the literature, the limited fields of view of *Chandra* and *XMM-Newton* mean that at $z < 0.1$, the available $L_X - kT$ relations were derived from earlier missions such as *ROSAT* and *ASCA*. For internal consistency, the $L_X - kT$ relation of the clusters in the sample with $0.1 < z < 0.2$ was fit as described above and used as the local baseline for our evolution study. In this fit, and all of the following evolution study, the core-excised properties were used. The parameters for the local $L_X - kT$ relation were $A_{LT} = (6.05 \pm 0.04) \times 10^{44} \text{ erg s}^{-1}$ and $B_{LT} = 2.51 \pm 0.29$.

For each cluster, the ratio of its observed luminosity to that predicted by self similar evolution of the local relation was computed, and termed Δ_L . Figure 10 shows the plot of Δ_L against redshift. In this plot, clusters following self-similar evolution would have $\Delta_L = 1$. Clusters more (less) luminous than predicted by the self-similar evolution of our local relation have $\Delta_L > 1$ ($\Delta_L < 1$). Figure 10 shows that relative to the local subset of clusters, those at intermediate redshifts ($0.2 < z < 0.6$) are significantly more luminous on average than the self-similar evolution model predicts. At high redshifts ($z > 0.6$) the clusters agree with the self-similar evolution model.

Similar results were reported by Branchesi et al. (2007, based in part on data from M08), and was suggested as evidence against the self-similar model. However, as noted by Branchesi et al. (2007), selection bias could be respon-

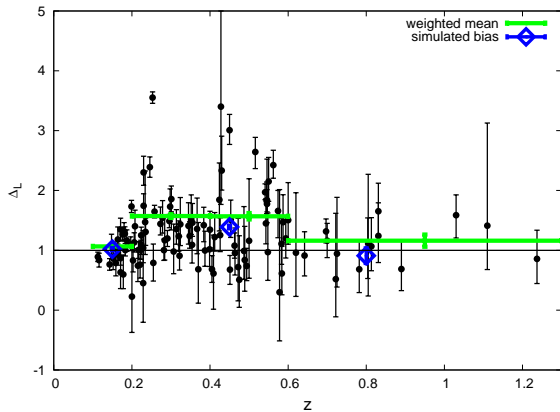


Figure 10. The ratio of the observed, core excised luminosity to that predicted by our local $L_X - kT$ relation, including self similar evolution, is plotted as a function of redshift. Clusters evolving self-similarly should scatter around $\Delta_L = 1$. Also shown are the weighted mean Δ_L in several redshift bins, and the possible effect on Δ_L due to Eddington bias in our simplistic bias simulations.

sible for distorting the observed evolution (see also §5.2 in Maughan 2007).

At this point, we note that there is some ambiguity in the terms used to describe different selection biases in the literature on cluster scaling relations, and so we pause for a brief discussion of selection bias and terminology.

5.1 Selection biases and terminology

We consider two types of bias that affect flux-selected samples of objects. Either or both of these biases are often referred to simply as “Malmquist bias” in the literature, while occasionally the term “Eddington bias” is also used. Teerikorpi (1997) gives a detailed overview of these selection biases and advocates the use of the terms Malmquist bias of the first and second kind. For clarity, we use the term “Malmquist bias” to refer to the effect that arises due to more luminous objects being detectable to greater distances, and “Eddington bias” to refer to the effect due to the differential scattering of objects across the threshold of a flux-limited sample. We will now discuss each of these biases in more detail in the following.

Let us consider a population of objects whose luminosities L are correlated to their masses M , with some intrinsic scatter in luminosity at a given mass (parametrised by $\sigma_{L|M}$). A sample of these objects whose measured flux is greater than some flux limit F_{lim} is then defined. In the idealised case where there is no scatter, the Malmquist bias will lead to the most massive, luminous objects being over-represented in the sample, due to the larger search volume in which they may be detected. This is easily corrected for with knowledge of the survey selection function [the survey volume as a function of luminosity; $V(L)$] to weight the objects by their search volume. In the more realistic case when there is scatter in L for fixed M , those objects with higher than average L for their mass, will be more numerous in the sample than those with lower than average L , again due to the larger survey volume. The mean luminosity of objects in

the sample is thus biased higher than the population average and the size of the bias depends on $\sigma_{L|M}$.

Turning now to the Eddington bias, let us consider objects close to the flux limit (by “close” we mean objects whose scatter in L has a non-negligible chance of moving them across the flux limit). Near the flux limit there exist objects whose mass corresponds to an average L that would be below the flux limit at their redshift, but whose observed L is higher than average, and so are included in the sample (we refer to these as overluminous). Similarly there exist objects whose mass corresponds to an average L that would be above the flux limit at their redshift, but whose observed L is lower than average, and so are not included in the sample (we refer to these as underluminous). This means that objects included in the sample are biased to above average L . So far, this is equivalent to a special case of the Malmquist bias, with the survey volume dropping to zero for objects whose observed luminosity is below the flux limit. What distinguishes the Eddington bias is an additional factor that arises when the number density of objects is a decreasing function of M and L (as is the case for galaxy cluster mass and luminosity functions). In this case, there are larger numbers of lower mass, overluminous objects which are included in the sample than higher mass, underluminous objects which drop out of the sample. This gives a further bias towards above-average luminosity in the final sample. The size of the Eddington bias depends on $\sigma_{L|M}$, and on the slope of the mass function at the mass whose average luminosity corresponds to the flux limit at the redshift in question.

In the above discussion, we assumed that $\sigma_{L|M}$ was due solely to an intrinsic dispersion in L at fixed M . Similar biases occur if L is subject to measurement errors. In this case, even in the absence of intrinsic variation of L at fixed M , there is an observed variation in L which has the same effect as the biases described above. A complicating factor is that the size of $\sigma_{L|M}$ will typically depend on L due to the larger measurement errors on fainter systems. This increases the difference between the number of overluminous objects moving into the sample from below the flux limit and underluminous objects moving out of the sample, further increasing the bias. If the objects are reobserved the average L will be unbiased for fixed M , as the original L values were randomly drawn from the possible L distribution (this is in contrast to the case where the variation in L at fixed M is intrinsic). The number of objects in the sample will remain biased, however, unless objects below the flux limit are also reobserved, and the sample redefined.

5.2 The effect of selection bias on cluster scaling relations

In studies of the evolving mass function of clusters based on X-ray flux limited samples, both the Malmquist bias and Eddington bias must be accounted for. Typically, the Malmquist bias as defined here is included in modelling the survey selection function, while the Eddington bias is taken into account when modelling the mass function (see e.g. Markevitch 1998; Vikhlinin et al. 2009a; Mantz et al. 2010b, for useful discussions of the effects of these biases). When X-ray selected clusters of galaxies are used for studying the scaling relation between L_X and another property (such as

kT), both the Malmquist and Eddington biases will enhance the mean L_X for a given kT (or mass). The effect of this can be to bias the normalisation of the $L_X - kT$ relation high, and bias the slope low. The effect on the slope arises because the lower temperature systems are closer to the flux limit at a given redshift, and so will suffer stronger bias. This effect is lessened if a wide redshift range is considered, as higher temperature objects will also tend to be close to the flux limit. As described above, the size of the total bias in the $L_X - kT$ relation will depend on $\sigma_{L|M}$, and on the slope of the mass function at the flux limit of the survey. Note that while $\sigma_{L|M}$ can be significantly reduced by excluding cluster cores for analysis purposes, the core-included L_X must be used in consideration of bias, as generally clusters are selected (or not) on the basis of their total L_X .

In the sample presented here, the clusters are drawn from a heterogeneous archive, and do not represent a statistically complete sample. However, most of the clusters were originally detected in X-ray surveys, and are thus subject to Malmquist and Eddington bias. A rigorous treatment of the bias is impossible without a well-defined selection function, but some simple simulations were performed to investigate the plausible effect that selection bias could have on the observed evolution of the $L_X - kT$ relation in this sample. The process used was to simulate a self-similar population of clusters, and apply selection functions representative of different cluster surveys. As discussed in Maughan (2007), we approximate the selection of clusters in our sample by three very broad classes of X-ray surveys: at low redshift ($z \approx 0.15$) many clusters were selected in shallow all-sky X-ray surveys, for which we use the Brightest Cluster Survey (BCS; Ebeling et al. 1998) flux limit as a template (a bolometric flux of $8.3 \times 10^{-12} \text{ erg s}^{-1} \text{ cm}^{-2}$); at moderate redshift ($z \approx 0.45$) most of the clusters come from deeper surveys for which we use the MACS (Ebeling, Edge & Henry 2001, ; bolometric flux limit of $3.4 \times 10^{-12} \text{ erg s}^{-1} \text{ cm}^{-2}$) as a template (our sample contains 24 MACS clusters with a median redshift of 0.42); at high redshifts ($z \approx 0.85$) most clusters in our sample were detected in deep surveys of *ROSAT* pointings, for which we use the WARPS (Scharf et al. 1997, bolometric flux limit of $9.1 \times 10^{-14} \text{ erg s}^{-1} \text{ cm}^{-2}$) as a template.

At each of the approximate redshifts corresponding to the above survey classes, a mass function was constructed using the model of Jenkins et al. (2001, see their Equation 9). This model is based on fitting results from cosmological simulations, and is similar in form to the standard Press-Schechter mass function (Press & Schechter 1974), although it provides a significantly improved fit to the simulations. The redshift range for each survey class was broken into smaller redshift bins, and clusters were drawn with random redshifts and masses (from the above mass function) until we obtained a set number of detected clusters within each bin (where a cluster is “detected” if its scattered total flux falls above the flux limit for the appropriate survey). The cluster luminosities were determined as follows. Each cluster was assigned a total (i.e. core included) luminosity $L_{X,\text{tot}}$ and a core excised luminosity $L_{X,c}$, using the $L_X - M$ relations of Maughan (2007). Importantly, these relations include self similar evolution, so the luminosity at fixed temperature evolves smoothly as $E(z)$. $L_{X,\text{tot}}$ was then randomised under a lognormal distribution with $\sigma = 39\%$ to give $L'_{X,\text{tot}}$,

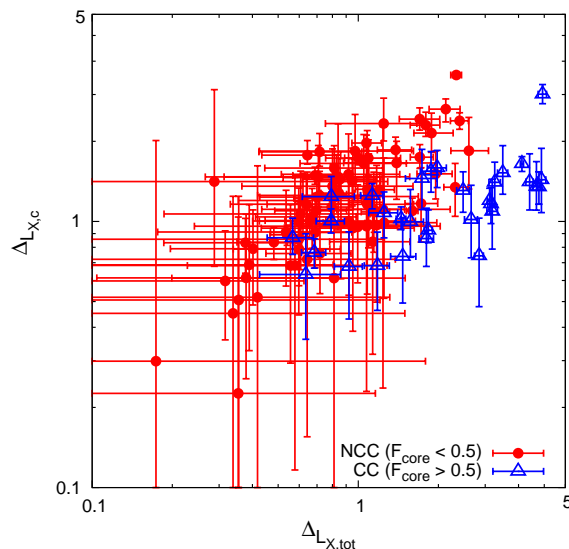


Figure 11. Plot showing the correlation between the ratio of observed to predicted L_X , when L_X and kT are measured with ($\Delta_{L_X,\text{tot}}$) and without ($\Delta_{L_X,c}$) the core regions included.

reproducing the intrinsic dispersion of the Maughan (2007) $L_{X,\text{tot}} - M$ relation. The value of $L_{X,c}$ was also shifted in the same direction by the same fractional amount but scaled by 17/39 (the ratio of the intrinsic scatters in the Maughan 2007, $L_{X,c} - M$ and $L_{X,\text{tot}} - M$ relations) to give $L'_{X,c}$. This gives consistent values of the total and core excised luminosities for each cluster, including intrinsic scatter. By scaling $L_{X,c}$ in this way, we are making the assumption that the dispersion in $L_{X,\text{tot}}$ is correlated with that in $L_{X,c}$. This is supported by Fig. 11, which shows $\Delta_{L_X,\text{tot}}$ plotted against $\Delta_{L_X,c}$ for the observed clusters (where $\Delta_{L_X,\text{tot}}$ is the ratio of the observed $L_{X,\text{tot}}$ to that predicted by the low-redshift $L_{X,\text{tot}} - kT$ relation, and $\Delta_{L_X,c}$ is the same but for core-excised quantities), and shows a positive correlation. The weak correlation for the CC clusters in the plot is testament to the efficacy of removing the core of those systems in reducing the dispersion in the $L_X - kT$ relation. Finally, for each cluster, a temperature was assigned, derived from the Vikhlinin et al. (2006b) $M - kT$ relation, again assuming self similar evolution, but neglecting any intrinsic scatter. Thus, at each of our redshifts of interest, we have produced a population of clusters whose observed properties ($L'_{X,\text{tot}}$, $L'_{X,c}$ and kT) are (by construction) described perfectly by a consistent set of self-similarly evolving scaling relations, with intrinsic dispersion in L_X .

The flux limit of each of our three representative surveys was converted to a luminosity limit at the appropriate redshift, and clusters with $L'_{X,\text{tot}}$ below that limit were rejected. In this way, the effects of the selection biases are reproduced. For the clusters surviving the survey selections, the ratio of $L'_{X,c}$ to $L_{X,c}$ was calculated, which corresponds to the Δ_L of the observed clusters. Figure 10 shows the mean Δ_L for the simulated clusters at each redshift. The departures from self similar evolution ($\Delta_L = 1$) are solely due to the selection biases, and as the intrinsic scatter $\sigma_{L|M}$ was constant with redshift in our simulations, the variation in Δ_L with redshift is simply due to the shape of the mass function close to the

flux limit of the different surveys and redshifts considered here.

6 DISCUSSION

6.1 Strong self-similarity

The examination of the slopes of the $L_X - kT$ relation in different sub-populations of this large cluster sample indicated that the most relaxed systems, or those hosting the strongest cool cores (definitions with significant overlap), exhibit a low scatter $L_X - kT$ relation with a slope of ≈ 2 , in agreement with the self-similar model, once their core regions have been excised. Such a self-similar correlation has generally not been found in previous studies of the $L_X - kT$ relation, which is likely due our large sample size, and to the fact that most previous studies have not distinguished CC and NCC subsamples once a core correction has been made. However, Pratt et al. (2009, hereafter P09) did make such a distinction in their recent *XMM-Newton* study of the $L_X - kT$ relation of the REXCESS sample, and used a similar methodology to us allowing straightforward comparisons to be made.

In the P09 study, after core exclusion, the $L_X - kT$ slopes of the relaxed/CC subsamples were shallower than the unrelaxed/NCC subsamples, but (in contrast to our results) were still significantly steeper than the self-similar slope of 2. The methods used to define the CC/NCC and relaxed/unrelaxed classes in P09 differ slightly from those employed here. P09 separated CC and NCC clusters using a measurement of the central density, and classed $\sim 30\%$ of their clusters as CC (a similar fraction to us). To classify relaxed and unrelaxed clusters, P09 used the same centroid shift measurement as us (albeit with a slightly different implementation), but used a value of $\langle w \rangle = 0.01R_{500}$ to segregate the relaxed/unrelaxed subsets. This less strict definition of a relaxed cluster than our $\langle w \rangle > 0.006R_{500}$, resulted in a significantly larger fraction of the P09 sample ($\sim 60\%$) being classed as relaxed.

Subsample definition and instrumentation notwithstanding, the key difference between the P09 and our samples is the temperature range of systems covered. Half of the P09 CC clusters are cooler than 3.5 keV (our coolest CC system). This is made clear in Figure 12, which plots the relaxed and CC P09 clusters on the corresponding $L_X - kT$ relations of our sample. At $kT \gtrsim 3.5$ keV the P09 data agree quite well with our $L_X - kT$ relations, with their essentially self-similar slopes (particularly for the CC selection). This suggests that the steeper P09 $L_X - kT$ slope is driven by their inclusion of lower mass systems, and that the self-similarity of relaxed/CC clusters found here is limited to more massive systems ($kT > 3.5$ keV).

Croston et al. (2008) presented the gas density profiles of the REXCESS clusters, allowing us to investigate if this possible similarity breaking of the $L_X - kT$ relation below 3.5 keV is manifested in the gas density profiles. In Fig. 13 we show the scaled gas density profiles of the CC REXCESS clusters, separated into hot ($kT > 3.5$ keV) and cool ($kT < 3.5$ keV) subsets. Also indicated is the mean profile of the relaxed clusters from our sample (as plotted in Fig 6). The hot REXCESS profiles agree fairly well with our mean

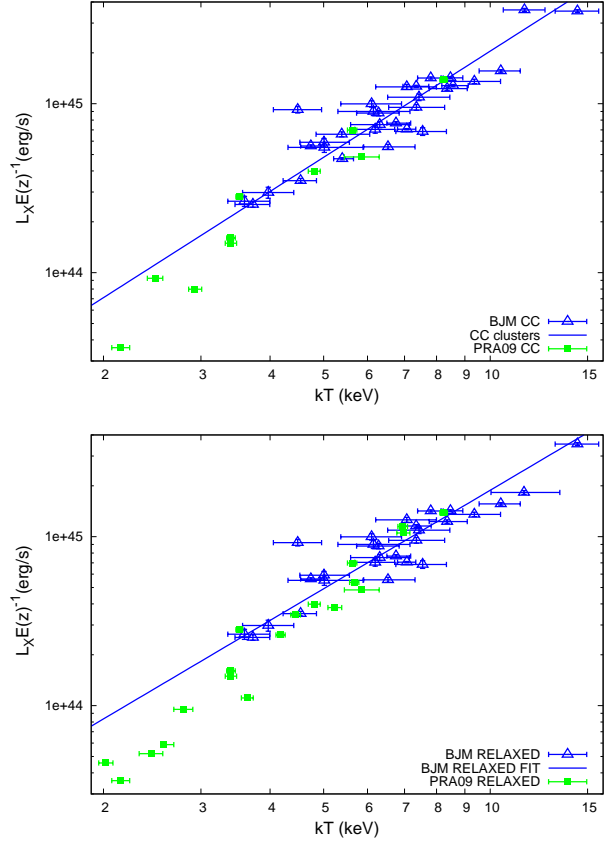


Figure 12. *Top:* the core-excised $L_X - kT$ relation for the CC clusters in the current sample is plotted along with the CC clusters of P09. *Bottom:* the core-excised $L_X - kT$ relation for the relaxed clusters in the current sample is plotted along with the relaxed clusters of P09.

relaxed profile (which are also all $kT > 3.5$ keV clusters), but the cool REXCESS CC clusters have flatter profiles, with lower gas densities than the other cluster profiles out to $\sim 0.7R_{500}$. This suggests that the self-similarity observed in the gas density profiles of the relaxed clusters in our sample is valid only for hotter ($kT > 3.5$ keV) systems. This is consistent with the proposed steepening of the $L_X - kT$ relation below 3.5 keV.

The scaled gas density profiles of our large sample also provide information on where self-similarity breaks down. For the unrelaxed/NCC clusters, these profiles showed that the similarity index was > 0 out to a cluster-centric radius of $\approx 0.7R_{500}$. Beyond this radius, the gas density profiles of the unrelaxed/NCC clusters appear self-similar. These results broadly agree with the *XMM-Newton* measurements of Croston et al. (2008, although in that work, clusters were not separated into relaxed/unrelaxed subsamples). In contrast, the similarity index of the relaxed/CC clusters is consistent with zero at all radii probed (Fig. 9). This would seem to imply that excluding the cores should not be required to recover a self-similar $L_X - kT$ relation. This may be the case, but as illustrated in Figures 8, while there is no strong temperature dependence of the scaled gas density in the cores, there is departure from self-similarity in the form of large cluster-to-cluster variation in scaled gas density. This is indicative of different cool core strengths

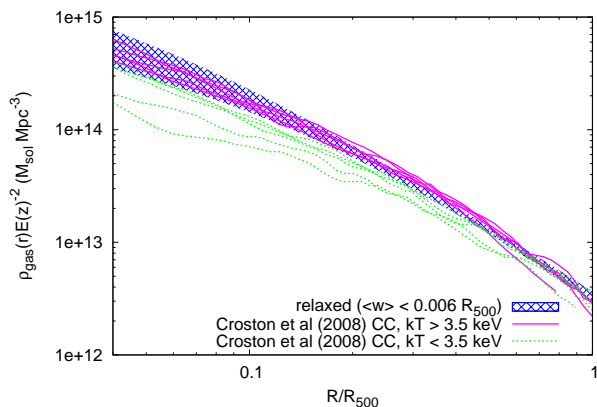


Figure 13. Scaled gas density profiles of the REXCESS CC clusters (taken from Croston et al. 2008). The REXCESS clusters are divided into hot and cool subsets as indicated. The hatched region indicated the standard deviation of the scaled gas density profiles of the relaxed clusters in our sample.

and is likely responsible for the non self-similarity of the core-included $L_X - kT$ relation. Finally, the REXCESS CC profiles in Fig. 13 show that in cool ($kT < 3.5$ keV) CC systems, the core gas density is lower than in hotter systems, suggesting that a non-zero similarity index would be measured at radii smaller than $\approx 0.7R_{500}$ for the relaxed/CC clusters in our sample if it included cooler systems.

Outside a radius of $\sim 0.15R_{500}$, the similarity index of relaxed/CC clusters is close to zero and the cluster-to-cluster variation in scaled gas density is low, indicating that the ICM in these regions is self-similar. This is consistent with the self-similar slope of the core-excised $L_X - kT$ relation of the relaxed/CC clusters.

Our results can also be usefully compared with the study by Mantz et al. (2010a) who found that when core regions were excised, the $L_X - kT$ relation slope was 2.70 ± 0.20 . Mantz et al. (2010a) did not separate relaxed and disturbed or CC/NCC clusters in their analysis, but their slope is in excellent agreement with the slope we find for all clusters with cores excised (2.72 ± 0.18). Usefully, Mantz et al. (2010a) were able to include full treatment of selection biases in their analysis, and showed that for core-excised luminosities, selection biases did not significantly impact the measured scaling relations, so the self-similar slope we find for the core-excised $L_X - kT$ relation of the relaxed/CC clusters in our sample is not likely to be affected by selection bias.

We thus conclude that the ICM of massive ($kT > 3.5$ keV), relaxed (or CC) clusters obeys strong self-similarity outside the core ($r < 0.15R_{500}$) regions.

6.2 Implications for similarity-breaking models

Pratt et al. (2010) argued that variations of the gas content of clusters with mass and radius are at the root of the observed departures from self-similarity of cluster entropy profiles. They proposed a mechanism whereby gentle heating from AGN, coupled with merger related mixing is responsible for a redistribution of gas, leading to the observed entropy profiles, and also the suppression of luminosity in low mass systems, giving rise to steepening in the $L_X - kT$

relation. Our results are consistent with this picture, but add the requirement that the most massive relaxed/CC systems are essentially self similar outside the central $0.15R_{500}$. The entropy of the CC clusters in the Pratt et al. (2010) sample shows evidence for excess above the self-similar expectations at radii as large as $\sim 0.7R_{500}$, however, this is driven by the lower mass systems. Clusters with $kT > 3.5$ keV are in reasonable agreement with the self-similar entropy model beyond $\sim 0.15R_{500}$ (roughly $0.1R_{200}$, as plotted in figure 3 in Pratt et al. 2010).

Our results on the details of the $L_X - kT$ relation and density structure of the ICM present new information with which to refine models of ICM heating and feedback. In particular, by identifying a fully self-similar regime in the cluster parameter space, we have a baseline against which to measure the impact of feedback.

Let us first consider the case of relaxed/CC clusters. With the core regions excluded, we find a self-similar $L_X - kT$ relation, which appears (when combined with the P09 data) to steepen below ~ 3.5 keV. The density profiles of the $kT > 3.5$ keV relaxed/CC systems are also self-similar beyond the core, with low dispersion and similarity index close to zero, but again the cooler REXCESS systems show similarity breaking, with suppressed densities relative to the hotter systems. Our results thus suggest that for relaxed systems above ~ 3.5 keV, the effects of feedback are negligible outside the core of $0.15R_{500}$.

A possible interpretation of this is that feedback occurs in the cores of all of the relaxed/CC systems, providing some fixed level of energy input beyond the balancing of the gas cooling. The heated gas will have raised entropy, and will rise, expand and cool, conserving entropy, until it reaches a radius of gas with the same entropy level. For more massive systems, this will occur at a smaller radius (see e.g. figure 1 in Pratt et al. 2010). Thus for a mass-independent amount of heating, there will be a mass threshold above which the effects of feedback are confined to the core regions. For a 3.5 keV system, the entropy level at $0.15R_{500}$ is ~ 200 keV cm^3 (Pratt et al. 2010), so an entropy increase somewhat lower than this would not redistribute gas much beyond the core. In the absence of mergers, the new entropy structure will remain intact until “eroded” by radiative cooling, but periodic core feedback would maintain a quasi-static ICM configuration.

For unrelaxed/NCC clusters, the population does not appear to be self-similar at any mass, even with the cores excluded. This is manifested in the steep $L_X - kT$ relation which crosses that of the relaxed/CC clusters at ~ 6 keV, and also in the gas density profiles, which show temperature dependence out to large scaled radii. The steepening of the $L_X - kT$ relation below 6 keV can be explained in the same terms as for the < 3.5 keV relaxed/CC clusters if we posit that core feedback occurs in all clusters (not just relaxed/CC) clusters. This is consistent with quasar mode heat input occurring in all clusters (Short & Thomas 2009). We then require that the effects of feedback be noticeable outside the core for more massive systems (up to $kT \approx 6$ keV). This requires a larger increase in entropy, as the ambient entropy level at $0.15R_{500}$ in a 6 keV system is ~ 300 keV cm^3 (Pratt et al. 2010). This is achievable in principal without additional feedback energy, via the amplification by merger shocks of entropy input in clus-

ter cores. This amplification is particularly effective if the original entropy increase was driven by lowering of the gas density rather than increasing its temperature (this effect is discussed in Ponman, Sanderson & Finoguenov 2003, in the context of the accretion of material during cluster formation). With the entropy further increased by merger shocks, the gas may then be able to settle to radii well beyond the cluster core. This model is similar to that proposed by Pratt et al. (2010), but with an emphasis on the role of mergers to amplify the entropy increase due to central energy input.

A challenge remains if we wish to explain all aspects of the observed departures from strong self-similarity in our sample with this central heating and merger shock mechanism: the loci of the > 6 keV unrelaxed/NCC clusters lie *above* the self-similar $L_X - kT$ relation. We thus speculate that while the combination of central heating and merger shocks may act to raise gas entropy beyond $0.15R_{500}$ in $kT < 6$ keV systems, at higher masses the dominant effect of mergers is to enhance L_X and/or suppress kT . We note that numerical simulations of clusters do not unambiguously support this hypothesis. Rowley, Thomas & Kay (2004) found that merging clusters tend to move along the $L_X - kT$ relation, though it was observed that L_X increases and kT decreases when the cores of two systems merge. A similar effect was also present in the merger simulations of Poole et al. (2007), in which massive $\gtrsim 6$ keV clusters were shown to have enhanced L_X relative to kT when the cores are at their closest initial approach, before settling down onto the $L_X - kT$ relation over a period of $\approx 4 - 5$ Gyr. This could explain the observed position of the unrelaxed clusters above the self-similar relation at the high- kT end, particularly combined with a selection bias to preferentially detect and observe clusters that are at the more luminous stages of their mergers (although we note that at a close core passage, such clusters may not be identified as unrelaxed).

By contrast, in the cosmological simulations of Hartley et al. (2008), mergers were found to push clusters along, but slightly below the mean $L_X - kT$ relation, leading to a curve towards a flatter $L_X - kT$ relation for disturbed clusters at the high kT end. This appears to contrast with our results, but the comparison is not straightforward, as the simulations are necessarily dominated by lower mass ($kT < 3$ keV) objects due to the limited volume simulated, and the classification of disturbed clusters is based on time since the last major merger, rather than a morphological measurement. For the same reasons, the results of these different computational studies are not necessarily at odds.

6.3 Heating or L_X suppression?

Given the loci of lower mass systems below the self-similar $L_X - kT$ relation, it is interesting to consider whether those clusters occupy that position due to their temperatures being enhanced relative to their virial temperature, or their luminosities being suppressed due to restructuring of the ICM. In some sense, this is just a question of timescales, as heating of a parcel of gas will eventually (on a timescale of order the sound-crossing time: a few 10^8 years; Mathews & Guo 2011) have risen, expanding and cooling, to its new adiabat, resulting in a restructuring of the ICM. Most theoretical work focuses on this longer term result of the re-

structured ICM, but some observational studies have argued that for clusters hosting radio-loud AGN, the steepening of the $L_X - kT$ relation is due to temperature enhancement of the ICM (Croston, Hardcastle & Birkinshaw 2005; Magliocchetti & Brüggen 2007).

In the absence of a coherent set of radio data for these clusters, we can appeal to their gas density profiles to investigate whether the steepening of the $L_X - kT$ relation is due to enhanced kT or suppressed L_X of the ICM. Fig. 13 shows that the ICM structure of the lower mass CC clusters is different from the self-similar higher mass CC profiles. The ICM density in the lower mass CC clusters is lower than or similar to the self-similar profiles, suggesting that the luminosity is suppressed in these systems by the removal of gas from the central regions out to R_{500} and beyond.

For *unrelaxed* clusters, Fig. 6 shows that their ICM structure is flatter than that of the self-similar relaxed clusters. Indeed, the gas density is higher for unrelaxed clusters at scaled radii $\gtrsim 0.4R_{500}$. A similar effect is seen in the scaled gas density profiles of the *Planck*-selected sample of largely unrelaxed clusters, when compared with the mean profile of the full REXCESS sample (Planck Collaboration et al. 2011). Indeed, the same excess of gas density at large radii in NCC clusters is also present (albeit more weakly) in the REXCESS profiles of (Croston et al. 2008) if they are separated into CC and NCC subsets. Given that the gas density is higher than the self-similar profiles at large scaled radii, it is not immediately clear if the net effect would be a suppression or increase of L_X . This can be crudely estimated by defining a “psuedo- L_X ” as the integral of the square of the scaled mean density profile over the spherical shell from $[0.15 - 1]R_{500}$. This calculation shows that the unrelaxed clusters have a mean luminosity $\sim 15\%$ lower than the relaxed clusters, so that the net effect of the observed ICM structural differences is suppression of L_X .

This picture changes slightly if the unrelaxed clusters are split into hot ($kT > 6$ keV) and cool ($kT < 6$ keV) subsets. The mean profiles of these subsets are shown in Fig. 14. The temperature dependence of the unrelaxed profiles is apparent, with cooler systems having a flatter mean profile, which crosses the mean relaxed profile at a larger scaled radius than the hotter unrelaxed systems. This is consistent with the picture of core feedback resulting in the removal of gas to larger radii in lower mass systems. The effect on the system luminosity is also different. For the hotter unrelaxed clusters, the psuedo- L_X is $\sim 5\%$ higher than the relaxed clusters, while for the cooler unrelaxed clusters it is $\sim 20\%$ lower. This is qualitatively consistent with the crossover of the relaxed/CC and unrelaxed/NCC $L_X - kT$ relations at 6 keV. For a quantitative comparison, the ratio of the luminosity predicted by the RCC and NRCC relations (Fig. 5) was computed for the temperature of each unrelaxed cluster. For the $kT < 6$ keV clusters, the mean ratio was 0.74, indicating that the 20% reduction in L_X suggested by the gas density profiles is sufficient to explain the steeper unrelaxed/NCC relation, without enhancement of the ICM temperature. For the $kT > 6$ keV unrelaxed clusters, the mean ratio was 1.30, significantly larger than the 5% increase in L_X predicted by the mean density profiles.

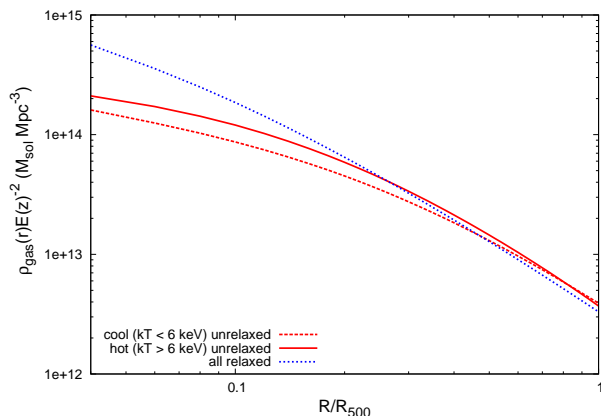


Figure 14. Average scaled gas density profiles of the relaxed and unrelaxed subsamples, with unrelaxed clusters subdivided into hot ($kT > 6$ keV) and cool ($kT < 6$ keV) subsets.

6.4 Weak self-similarity

Our investigation of the evolution of the $L_X - kT$ relation suggests at first glance, a set of clusters at intermediate redshifts ($0.2 < z < 0.6$) with luminosities significantly higher than predicted by self-similar evolution of the low-redshift relation (Figure 10). This is similar to the results of Branchesi et al. (2007), who argued in favour of non self-similar evolution. Our simple simulations of a self-similar population of clusters subjected to selection functions that plausibly approximate those of our heterogeneously selected sample indicated that the deviations from self-similarity can reasonably be explained by selection biases. As demonstrated by the simulations, the combination of intrinsic scatter $\sigma_{L|M}$, and the slope of the mass function at the mass corresponding to the survey flux limit give differing amounts of bias for different flux limit and redshift combinations. We thus find no evidence to reject the self-similar description of evolution in the $L_X - kT$ relation. This conclusion is in agreement with other analyses based on statistically complete samples where full treatment of selection effects is possible (Pacaud et al. (2007, 29 clusters at $z \lesssim 1$) Mantz et al. (2010a, 238 clusters at $z \lesssim 0.5$)) which found no strong evidence for departures from self-similar evolution in the $L_X - kT$ or $L_X - M$ relation (although we note that in a similar analysis, Vikhlinin et al. 2009a, found an indication of evolution slightly weaker than the self-similar prediction for the $L_X - M$ relation).

Our simple simulations assumed $\sigma_{L|M}$ was constant with redshift, but in fact this may not be the case. Maughan (2007) showed that $\sigma_{L|M}$ was significantly lower for the clusters in the current sample at $z > 0.5$ than those at $z < 0.5$. This is consistent with evidence that the fraction of clusters with cool cores (the dominant contributor to $\sigma_{L|M}$) decreases strongly above $z \approx 0.5$ (Vikhlinin et al. 2006a). Evolution in $\sigma_{L|M}$ could introduce further bias in measurements of the $L_X - kT$ relation evolution. This evolution of the CC clusters was investigated in our sample, and Figure 15 shows normalised histograms of F_{core} for $z \geq 0.5$ and $z < 0.5$ clusters.

Fig. 15 shows a clear absence of strong CC ($F_{\text{core}} > 0.5$) clusters at $z > 0.5$ in the current sample. A similar trend is seen in the simulations of Kay et al. (2007), who found

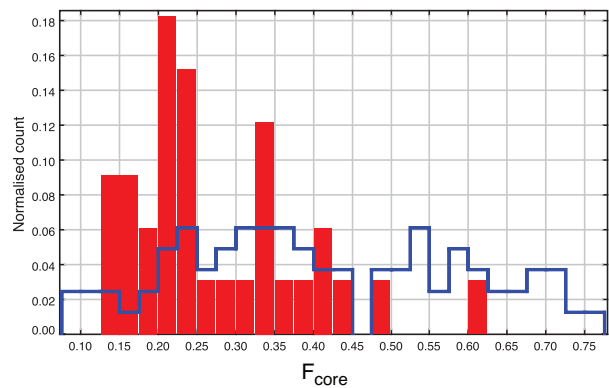


Figure 15. Histogram of F_{core} values for clusters at $z < 0.5$ (lines) and $z \geq 0.5$ (filled bars). Each histogram is normalised to unity.

a corresponding reduction in $\sigma_{L|T}$ with redshift. Our results agree with the Vikhlinin et al. (2006a) findings, and we also found similar histograms when using the cuspiness CC proxy. We also showed previously that the fraction of relaxed clusters decreased significantly at $z > 0.5$ in the current sample (Maughan 2007). However, while these results provide strong evidence for evolution in the CC population in our sample, we remind the reader once more of the heterogeneous nature of our sample and urge caution in extrapolating these results to the general cluster population (see e.g. Sanderson, O’Sullivan & Ponman 2009; Mittal et al. 2011, for discussions of cool core properties in representative samples). Indeed, even in statistically complete samples, the fraction of CC clusters at high redshift is subject of some debate. Santos et al. (2010) recently showed that the cool core fractions in three high-redshift *ROSAT*-derived surveys differed significantly, most likely due to their different cluster detection algorithms (high- z cool core clusters could be classed as point sources and excluded from samples). In two of the surveys considered, the distribution of CC strengths (measured with a method similar to our F_{core} proxy) was similar at low and high ($z > 0.6$) redshift. This would imply weaker (or zero) evolution in $\sigma_{L|M}$ than found in our non-representative sample. The uncertainty on the evolution in $\sigma_{L|M}$ further complicates attempts to fully include selection bias corrections in studies of the evolution in the $L_X - kT$ relation, although note that Vikhlinin et al. (2009a) showed that estimates of $\sigma_{L|M}$ from flux-limited samples are unbiased, making bias-corrected studies feasible.

The redshift evolution of the relaxed/CC fraction in our sample means that the relaxed/CC and unrelaxed/NCC subsets cover different redshift ranges with the relaxed/CC subsets essentially limited to $z < 0.5$. In order to test whether this difference contributed to the shallower $L_X - kT$ slopes found for the relaxed/CC clusters, the $L_X - kT$ relations of the unrelaxed/NCC clusters were fit for $z < 0.5$ and $z \geq 0.5$ clusters separately. The slopes of both the high and low redshift unrelaxed/NCC clusters agreed very well with the fit to the full unrelaxed/NCC subsample, and there was no evidence for a change of slope with redshift.

7 CONCLUSIONS

We have used a sample of 114 clusters observed with *Chandra* ACIS-I across a wide baseline in temperature ($2 < kT < 16$ keV) and redshift ($0.1 < z < 1.3$) to study the self similarity of the cluster population in terms of its mass scaling and redshift evolution. Our main conclusions on the mass scaling of the clusters are as follows:

- The ICM of massive ($kT > 3.5$ keV), relaxed/CC galaxy clusters is self-similar outside of the central $0.15R_{500}$. In this regime, strong self-similarity is obeyed, manifested in an $L_X - kT$ relation with a slope of ≈ 2 , and ICM density profiles with low dispersion and no temperature dependence.
- By comparing our data with measurements of the REXCESS sample, which extends to lower masses, we find that the self similarity of the relaxed/CC clusters breaks below ~ 3.5 keV, manifested by a steepening $L_X - kT$ relation and flatter density profiles. This implies that the impact of central heating extends beyond the core in these lower mass systems.
- Unrelaxed/NCC clusters are not self-similar; their $L_X - kT$ relation has a steeper than self-similar slope, and their ICM density profiles are temperature-dependent out to $\approx 0.7R_{500}$.
- The steeper unrelaxed/NCC core-excised $L_X - kT$ relation crosses the self-similar relaxed/CC relation at around 6 keV. Below this temperature unrelaxed/NCC clusters appear to be less luminous than their relaxed/CC counterparts, while above this temperature they appear to be cooler and/or more luminous.
- These results are consistent with similarity breaking in clusters being due to central feedback, the effects of which extend beyond the central $0.15R_{500}$ in low mass ($\lesssim 3.5$ keV) systems. We suggest that merger shocks act to amplify the entropy increase from this feedback, allowing its effect to be felt beyond the core in more massive ($\lesssim 6$ keV) unrelaxed systems. In the most massive systems, any heating is limited to the core regions and the dominant effect of mergers is to raise the luminosity of the ICM or lower its temperature relative to the self-similar $L_X - kT$ relation.

Our investigation of the evolution of the $L_X - kT$ relation gave the following main results:

- The evolution of the $L_X - kT$ relation in our sample is inconsistent at face value with the self-similar model, but these differences are plausibly explained by a reasonable model of the varying selection biases due to the different selection functions in place across our heterogeneous sample.
- Our bias modelling assumed the intrinsic scatter in the $L_X - M$ relation ($\sigma_{L|M}$) is redshift independent, however, in our sample the fraction of cool core clusters is much lower at $z > 0.5$, consistent with the smaller $\sigma_{L|M}$ we found at $z > 0.5$ for the same clusters in Maughan (2007). Such variation in $\sigma_{L|M}$ could further bias evolution measurements, but should be applied to the general population with caution due to the non-representative nature of our sample.
- We would thus argue that for the core-excised $L_X - kT$ relation, self-similar evolution is obeyed to at least a first order approximation. This suggests that the balance of heating, cooling and mergers has remained roughly constant since $z \sim 1$. Stronger constraints on non self-similar be-

haviour require statistically complete samples at all redshifts, with a full treatment of the selection function, including the sensitivity of the cluster detection algorithm to cool core clusters at high redshift.

Current X-ray surveys such as XXL (Pierre et al. 2010), XCS (Lloyd-Davies et al. 2010), and XDCP (Fassbender 2008) are beginning to produce suitable samples to study cluster evolution on a stronger statistical foundation, extending the work of Mantz et al. (2010a) and Vikhlinin et al. (2009a) to $z > 1$. Further insight will be gained by studies of samples selected independently of the X-ray emission such as optical, weak lensing, and to some extent the Sunyaev-Zel'dovich effect (SZE; although the X-ray properties of SZE selected clusters may retain some bias due to the dependence of both on the physical properties of the ICM).

8 ACKNOWLEDGEMENTS

We thank Trevor Ponman, Alastair Sanderson and Gabriel Pratt for useful discussions of this work. The financial support for SWR was partially provided for by the Chandra X-ray Center through NASA contract NAS8-03060, and the Smithsonian Institution.

REFERENCES

- Akritas M. G., Bershadsky M. A., 1996, *ApJ*, 470, 706
 Allen S. W., Rapetti D. A., Schmidt R. W., Ebeling H., Morris R. G., Fabian A. C., 2008, *MNRAS*, 383, 879
 Arnaud M., Aghanim N., Neumann D. M., 2002, *A&A*, 389, 1
 Arnaud M., Pratt G. W., Piffaretti R., Böhringer H., Croston J. H., Pointecouteau E., 2010, *A&A*, 517, A92+
 Borgani S., Governato F., Wadsley J., Menci N., Tozzi P., Quinn T., Stadel J., Lake G., 2002, *MNRAS*, 336, 409
 Bower R. G., 1997, *MNRAS*, 288, 355
 Bower R. G., McCarthy I. G., Benson A. J., 2008, *MNRAS*, 390, 1399
 Branchesi M., Gioia I. M., Fanti C., Fanti R., 2007, *A&A*, 472, 739
 Bryan G. L., 2000, *ApJ*, 544, L1
 Bryan G. L., Norman M. L., 1998, *ApJ*, 495, 80
 Croston J. H., Hardcastle M. J., Birkinshaw M., 2005, *MNRAS*, 357, 279
 Croston J. H. et al., 2008, *A&A*, 487, 431
 David L. P., Nulsen P. E. J., McNamara B. R., Forman W., Jones C., Ponman T., Robertson B., Wise M., 2001, *ApJ*, 557, 546
 Dickey J. M., Lockman F. J., 1990, *ARA&A*, 28, 215
 Ebeling H., Edge A. C., Böhringer H., Allen S. W., Crawford C. S., Fabian A. C., Voges W., Huchra J. P., 1998, *MNRAS*, 301, 881
 Ebeling H., Edge A. C., Henry J. P., 2001, *ApJ*, 553, 668
 Edge A. C., Stewart G. C., 1991, *MNRAS*, 252, 414
 Ettori S., Tozzi P., Borgani S., Rosati P., 2004, *A&A*, 417, 13
 Fabian A. C., 1994, *ARA&A*, 32, 277
 Fassbender R., 2008, *astro-ph/0806.0861*

- Hartley W. G., Gazzola L., Pearce F. R., Kay S. T., Thomas P. A., 2008, *MNRAS*, 386, 2015
- Helsdon S. F., Ponman T. J., 2000, *MNRAS*, 315, 356
- Hudson D. S., Mittal R., Reiprich T. H., Nulsen P. E. J., Andernach H., Sarazin C. L., 2010, *A&A*, 513, A37+
- Jenkins A., Frenk C. S., White S. D. M., Colberg J. M., Cole S., Evrard A. E., Couchman H. M. P., Yoshida N., 2001, *MNRAS*, 321, 372
- Kaastra J. S., Ferrigno C., Tamura T., Paerels F. B. S., Peterson J. R., Mittaz J. P. D., 2001, *A&A*, 365, L99
- Kaiser N., 1986, *MNRAS*, 222, 323
- Kay S. T., da Silva A. C., Aghanim N., Blanchard A., Liddle A. R., Puget J.-L., Sadat R., Thomas P. A., 2007, *MNRAS*, 377, 317
- Kravtsov A. V., Vikhlinin A., Nagai D., 2006, *ApJ*, 650, 128
- Lloyd-Davies E. J. et al., 2010, *astro-ph/1010.0677*
- Lumb D. H. et al., 2004, *A&A*, 420, 853
- Magliocchetti M., Brüggemann M., 2007, *MNRAS*, 379, 260
- Mantz A., Allen S. W., Ebeling H., Rapetti D., Drlica-Wagner A., 2010a, *MNRAS*, 406, 1773
- Mantz A., Allen S. W., Rapetti D., Ebeling H., 2010b, *MNRAS*, 406, 1759
- Markevitch M., 1998, *ApJ*, 504, 27
- Mathews W. G., Guo F., 2011, *astro-ph/1105.5870*
- Maughan B. J., 2007, *ApJ*, 668, 772
- Maughan B. J., Jones C., Forman W., Van Speybroeck L., 2008, *ApJS*, 174, 117
- Maughan B. J., Jones L. R., Ebeling H., Scharf C., 2006, *MNRAS*, 365, 509
- McCarthy I. G., Schaye J., Bower R. G., Ponman T. J., Booth C. M., Dalla Vecchia C., Springel V., 2011, *MNRAS*, 35
- McNamara B. R., Nulsen P. E. J., 2007, *ARA&A*, 45, 117
- Mitchell R. J., Dickens R. J., Burnell S. J. B., Culhane J. L., 1979, *MNRAS*, 189, 329
- Mittal R., Hicks A., Reiprich T. H., Jaritz V., 2011, *astro-ph/1106.5185*
- Mushotzky R. F., 1984, *Physica Scripta Volume T*, 7, 157
- Neumann D. M., Arnaud M., 1999, *A&A*, 348, 711
- Nord B., Stanek R., Rasia E., Evrard A. E., 2008, *MNRAS*, 383, L10
- Osmond J. P. F., Ponman T. J., 2004, *MNRAS*, 350, 1511
- Pacaud F. et al., 2007, *MNRAS*, 382, 1289
- Peterson J. R. et al., 2001, *A&A*, 365, L104
- Pierre M., Pacaud F., Juin J. B., Melin J. B., Clerc N., Corasaniti P. S., 2010, *astro-ph/1009.3182*
- Planck Collaboration et al., 2011, *astro-ph/1101.2025*
- Ponman T. J., Cannon D. B., Navarro J. F., 1999, *Nature*, 397, 135
- Ponman T. J., Sanderson A. J. R., Finoguenov A., 2003, *MNRAS*, 343, 331
- Poole G. B., Babul A., McCarthy I. G., Fardal M. A., Bildfell C. J., Quinn T., Mahdavi A., 2007, *MNRAS*, 380, 437
- Poole G. B., Fardal M. A., Babul A., McCarthy I. G., Quinn T., Wadsley J., 2006, *MNRAS*, 373, 881
- Pratt G. W. et al., 2010, *A&A*, 511, A85+
- Pratt G. W., Croston J. H., Arnaud M., Böhringer H., 2009, *A&A*, 498, 361
- Press W. H., Schechter P., 1974, *ApJ*, 187, 425
- Randall S. W., Sarazin C. L., Ricker P. M., 2002, *ApJ*, 577, 579
- Reese E. D., Kawahara H., Kitayama T., Ota N., Sasaki S., Suto Y., 2010, *ApJ*, 721, 653
- Rowley D. R., Thomas P. A., Kay S. T., 2004, *MNRAS*, 352, 508
- Sanderson A. J. R., O'Sullivan E., Ponman T. J., 2009, *MNRAS*, 395, 764
- Santos J. S., Tozzi P., Rosati P., Böhringer H., 2010, *A&A*, 521, A64+
- Scharf C., Jones L. R., Ebeling H., Perlman E., Malkan M., Wegner G., 1997, *ApJ*, 477, 79
- Short C. J., Thomas P. A., 2009, *ApJ*, 704, 915
- Short C. J., Thomas P. A., Young O. E., Pearce F. R., Jenkins A., Muanwong O., 2010, *MNRAS*, 408, 2213
- Smith R. K., Brickhouse N. S., Liedahl D. A., Raymond J. C., 2001, *ApJ*, 556, L91
- Stanek R., Evrard A. E., Böhringer H., Schuecker P., Nord B., 2006, *ApJ*, 648, 956
- Teerikorpi P., 1997, *ARA&A*, 35, 101
- Vikhlinin A., Burenin R., Forman W. R., Jones C., Hornstrup A., Murray S. S., Quintana H., 2006a, *astro-ph/0611438*
- Vikhlinin A. et al., 2009a, *ApJ*, 692, 1033
- Vikhlinin A., Kravtsov A., Forman W., Jones C., Markevitch M., Murray S. S., Van Speybroeck L., 2006b, *ApJ*, 640, 691
- Vikhlinin A. et al., 2009b, *ApJ*, 692, 1060
- Vikhlinin A., Markevitch M., Murray S. S., Jones C., Forman W., Van Speybroeck L., 2005, *ApJ*, 628, 655
- Vikhlinin A., VanSpeybroeck L., Markevitch M., Forman W. R., Grego L., 2002, *ApJ*, 578, L107
- Voit G. M., Kay S. T., Bryan G. L., 2005, *MNRAS*, 364, 909